City Research Online

City, University of London Institutional Repository

Citation: Karathanassis, I. K., Papanicolaou, E., Belessiotis, V. & Bergeles, G. (2013). Three-dimensional flow effects on forced convection heat transfer in a channel with stepwise-varying width. International Journal of Thermal Sciences, 67, pp. 177-191. doi: 10.1016/j.ijthermalsci.2012.12.016

This is the accepted version of the paper.

This version of the publication may differ from the final published version.

Permanent repository link: http://openaccess.city.ac.uk/18286/

Link to published version: http://dx.doi.org/10.1016/j.ijthermalsci.2012.12.016

Copyright and reuse: City Research Online aims to make research outputs of City, University of London available to a wider audience. Copyright and Moral Rights remain with the author(s) and/or copyright holders. URLs from City Research Online may be freely distributed and linked to.

City Research Online: http://openaccess.city.ac.uk/ publications@city.ac.uk

Three-dimensional flow effects on forced convection heat transfer in a channel with stepwise-varying width.

I.K. Karathanassis[a, b,*], E. Papanicolaou[a], V. Belessiotis[a] and G.C. Bergeles[b]

[a]Solar & other Energy Systems Laboratory, Institute of Nuclear Technology & Radiation Protection, National Centre for Scientific Research DEMOKRITOS, Aghia Paraskevi, 15310 Athens, Greece

[b]Laboratory of Innovative Environmental Technologies, School of Mechanical Engineering, National Technical University of Athens, Zografos Campus, 15710 Athens, Greece

[*] Corresponding author. E-mail address: ikarathanassis@ipta.demokritos.gr (I. K. Karathanassis).

Abstract. A numerical investigation based on the finite volume methodology of the three-dimensional laminar flow and conjugate heat transfer inside a plate-fin heat sink with stepwise-varying channel width is presented. Results are obtained for the three-dimensional flow developed in the vicinity of the flow contraction as manifested by the existence of two pairs of contra-rotating longitudinal vortices, one at the corners of the fin leading edge and the other at the flow separated regions. The topology of the flow is thoroughly examined and the contributions of the endwalls and the front surface of the flow-contracting fin to the mechanisms that cause the emergence of the three-dimensionality are determined. It is established that the corner longitudinal vortices are in fact horseshoe vortices, which emerge due to the deceleration effect of the fin front surface on the oncoming fluid. Furthermore, the interaction between the corner longitudinal vortices and the downstream recirculation bubble formed over the fin tip is also elucidated. The analysis covers a wide range of flow conditions within the laminar region in order to monitor the effect of the Reynolds number on the flow topology and to verify that the flow remains symmetrical in this region. From the numerical results, it is deduced that the recirculation downstream of the flow contraction has a beneficial impact on the heat sink thermal performance, a fact quantified through the local Nusselt number distributions.

Keywords: flow contraction, stepwise-varying width, secondary-flow pattern, horseshoe vortex, plate-fin heat sink

Nomenclature

A	area, m^2
AR	aspect ratio, $AR = \frac{H_{ch}}{B_{ch}}$
B	width, m
BR	blockage ratio, $BR = \frac{B_w}{B_{ch,1}}$

C_p	pressure coefficient $C_p = \dfrac{p - p_{ref}}{1/2 \rho w_i^2}$
D_h	hydraulic diameter of heat sink section i (i=1,2) $D_{h,i} = \dfrac{2B_{ch,i}H_{ch}}{(B_{ch,i} + H_{ch})}$, m
e	heat transfer to pressure drop ratio $e = \dfrac{\bar{h}/\bar{h}_0}{\Delta p/\Delta p_0}$
Gr	Grashof number in heat-sink section i (i=1,2), $Gr_i = \dfrac{g\beta q'' D_{h,i}^4}{\nu^2 k_f}$
H	overall heat sink height $H = H_{ch} + t_s$, m
H_{ch}	channel height, m
h	heat transfer coefficient $h = \dfrac{-k(\partial T/\partial n)_w}{(T_w - T_{f,m})}$, W/m^{2}K
k	thermal conductivity, W/mK
L	length, m
$L_{X,r}^*, L_{Y,r}^*, L_{Z,r}^*$	non-dimensional reattachment length $L_r^* = \dfrac{l_r}{B_w}$
Nu	Nusselt number in heat sink section i (i=1,2), $Nu = \dfrac{h \cdot D_{h,i}}{k_f}$
p	pressure, Pa
p_{ref}	pressure at the channel mid-length (L/2) for undisturbed parallel flow
P	channel perimeter, m
q''	heat flux, W/m^2
Re	Reynolds number in heat sink section i (i=1,2), $Re_i = \dfrac{w_{m,i} D_{h,i}}{\nu}$,
T	temperature, K
T^*	non-dimensional temperature $T^* = \dfrac{T - T_{f,i}}{T_{max} - T_{f,i}}$
T_{max}	maximum heat-sink temperature, K
t_s	solid substrate thickness, m
$\dot{V}$	volumetric flow rate, m^3/s
W	width, m
w	flow axial velocity, m/s
x,y,z	streamwise, vertical and spanwise coordinate respectively, m
X^*	non-dimensional spanwise coordinate, $X^* = \dfrac{x}{B_{ch,2}} - \dfrac{1}{2}$
Y^*	non-dimensional height-wise coordinate, $Y^* = \dfrac{y - t_s}{H_{ch}}$

Z^*	non-dimensional streamwise coordinate, $Z^* = \frac{z - z_0}{D_{h,1}}$
z_0	location of the flow contraction, z_0=0.25m

Greek symbols

μ	dynamic viscosity, Pa·s
ν	kinematic viscosity, m^2/s
ρ	density, kg/m^3
ω	vorticity $\vec{\omega} = \vec{\nabla} \times \vec{\upsilon}$, s^{-1}

Subscript

ave	average
ch	channel
cs	cross section
f	fluid
FD	fully developed
hs	heat sink
i	inlet
init	initial
int	interface
m	mean
r	reattachment
s	solid, section
sep	separation
st	step
tot	total
w	wall
0	value for parallel flow

1. Introduction

Flow separation and consequent reattachment arises in several engineering applications. In heat transport processes, flow separation has a significant impact on the performance of heat exchanging devices such as cooling systems for electronic components, combustion chambers and turbine blades, as well as receivers of concentrating solar collectors. Thus, the specification of geometrical configurations that provoke flow separation and secondary flows is an important part of the design procedure of such devices.

The most commonly cited geometrical configurations, where flow separation with accompanying reattachment and redevelopment occurs, comprise the backward and forward-facing step and the flows around various types of bluff bodies, for instance, surface mounted elongated obstacles such as plates or fins. Regarding these configurations, a number of researchers [1-4] focused their investigations on the two-dimensional characteristics of the separated flow, both in the laminar and the turbulent region, with the backward-facing step case to be considered as a benchmark problem for validating numerical codes [2].

The two-dimensional flow over a forward-facing step exhibits three characteristic regions: a separation zone adjacent to the step salient corner, a recirculation zone at the step tip, and a re-attachment section downstream of the step. It is reported, [3,4], that although the salient corner vortex is formed even for creeping flows, the tip vortex is detected after a critical value of the Reynolds number. The formation of the separation bubble immediately downstream of the leading edge is a feature also encountered in the flow around blunt plates. The studies of Djilali [5] and Rahnema et al. [6] were focused on the two-dimensional laminar steady flow around an array of plates and demonstrated two main findings: the linear increase of the separation bubble length with the Reynolds number (for a constant blockage ratio) and the significant heat transfer augmentation in the reattachment region. Marty et al. [7] expanded the two-dimensional steady-flow calculations to unsteady flow as well. They reported that the heat transfer for high Re numbers was enhanced by 50% in comparison to an infinite plate due to the unsteadiness of the recirculation bubble and they confirmed their numerical predictions by experimental measurements.

The three-dimensional nature of separated flows in the case of a geometrical confinement generates a complex velocity field manifested by the formation of distinct vortex structures [8-11]. Stüer et al. [8] used the hydrogen bubble technique and particle tracking velocimetry to visualize the laminar three-dimensional flow ahead of a forward facing step. Their experiments were conducted in an open water channel, wide enough to exclude the side walls influence; it was concluded that the separation bubble at the step base corner is of the open type and that the entrained fluid, after executing a helical movement in the spanwise direction, is released over the step and transformed to a longitudinal vortex in a quasi-periodic manner. A similar observation was made by Largeau and Moriniere [9] who experimentally examined turbulent air flow over a forward facing step in an open channel. They noticed a structure similar to a horseshoe vortex in front of the step and came to the conclusion that the flow passes the step over paths of approximately the same spanwise distance. Wilhelm et al. [10] performed a computational analysis of the three-dimensional, laminar, incompressible flow of a Newtonian fluid over an infinite, in the spanwise direction, forward-facing step. The simulation was initialized with a two-dimensional solution and three-dimensional perturbations of different kind and intensity were superimposed. The formation of pairs of longitudinal counter-rotating vortices downstream of the step was established and it was remarked that a characteristic sequence of streaks also appeared downstream of the step, which marked the paths of fluid entrainment over the step. The topology of this streaky pattern was found to be closely related to the longitudinal vortices, as a periodic pair of counter rotating vortices was always located between two paths of fluid entrainment. Barbosa-Saldaña et al. [11] also investigated numerically the three-dimensional laminar forward-facing step flow using a finite volume method. They examined the effect of increased Reynolds number on the magnitude and location of the salient and tip vortices detected immediately upstream and at the edge of the step respectively, but they did not mention the emergence of any periodic longitudinal vortices.

Yaghoubi et al. [12] in their numerical investigation of the three-dimensional turbulent air flow and conjugate heat transfer around an array of rectangular parallel plates of finite thickness established that the flow was symmetric in that configuration and consequently conducted their computations with respect to various plate geometrical parameters (aspect ratio, blockage ratio and spacing) on a reduced domain containing a half-section of the plate. The authors concluded their study by

numerically deriving analytical correlations regarding the reattachment length and the overall Nusselt number. It was accentuated that the overall Nusselt number increases with the blockage ratio.

Zhang et al. [13] conducted a numerical analysis in order to capture the topology of the unsteady three-dimensional flow around cascading blunt-plate arrays. The effect of the end walls was not taken into consideration as periodic conditions were imposed along all directions. The emergence of longitudinal vortices was established, which were furthermore found to interact and extract energy from the spanwise vortices that constitute a two-dimensional feature of the flow. Yanaoka et al. [14] numerically investigated the three-dimensional laminar fluid flow and heat transfer around a blunt plate inside a square channel in order to point out the effects of the lateral walls. The blockage ratio defined as the ratio of the plate thickness to the channel width was equal to 10%. An interesting result of the study was the detection of a horseshoe vortex in the vicinity of the side wall downstream of the plate edge that leads to a thinning of the thermal boundary layer in that region and significant enhancement of the local Nusselt number values. For Re=450 (based on the plate thickness) the flow became unsteady and a single hairpin vortex with a spanwise scale of approximately twice the plate thickness was formed downstream of the plate leading edge.

The horseshoe vortex is a pattern also encountered in flows around unconfined surface mounted obstacles. Nakamura et al. [15] visualized the turbulent air flow around a 30mm cube using an oil-film method. They noticed the formation of the horseshoe pattern on the floor adjacent to both the front and side regions of the cube. It was also stated that the heat transfer on the base wall was significantly enhanced because of the influence of the vortex. The formation of the horseshoe vortex at the leading face of an obstacle was also observed by Meinders and Hanjalić [16] who visualized the air flow around a matrix of equidistant cubes.

The three-dimensional characteristics of a flow undergoing an abrupt contraction inside a rectangular confined geometry under forced convection conditions are investigated in this work. A common practice to enhance the thermal performance of a heat exchanging configuration is to increase the total heat exchanging area using fins or multiple passages of the cooling fluid. Based on this concept, the heat sink under investigation comprises a series of rectangular channels that sustain an abrupt width reduction at the configuration mid-length. The first objective of the present study is to scrutinize the effect of the contraction on the flow field by illustrating the topology of the emerging vortical structures and identifying the mechanisms that cause their onset. Subsequently, the influence of the developing secondary-flow pattern on the temperature field and the overall heat transfer rate of the heat sink is investigated. The numerical results are presented for three values of the Reynolds number (Re_1=519,1038,1557) that cover the entire laminar steady flow region.

2. Geometry

The heat sink design to be addressed by the present study (Fig. 1) comprises a series of rectangular channels with a stepwise width reduction occurring midway along their length. This design concept was first implemented by Barrau et al. [17] in a jet impingement cooling device. In this concept, the total length of the heat sink is divided into distinct consecutive sections, whereby the downstream section has twice the number of channels of the upstream one. This conceptual design can ideally be further developed into (*dendritic*) tree-like structures with enhanced thermal

performance, by adding more sections with channel widths that extend down to the microscale. However, the increasing complexity of such a structure also leads to prohibitively high manufacturing costs, which is a hindering factor for the use of such heat sinks in practical applications. Therefore, this study refers to the simplest, two-section configuration, which is adequate for the investigation of the three-dimensional flow features in the transition between two consecutive sections of the heat sink.

The proposed heat sink configuration is primarily directed for use at concentrating photovoltaic/thermal (CPVT) applications [18] and has a total area of 500 mm x 60 mm. The fluid enters the heat sink in parallel flow and branches into the subsequent channel sections. The total number of the parallel channels N in the each section can be determined by the following relationship, depending on the channel width and the wall thickness

$$N_i = \frac{B_{hs} - a_i B_{ch,i}}{(a_i + 1) B_{ch,i}} \tag{1}$$

where $a=B_w/B_{ch}$, B_{hs} is the total heat sink width, B_{ch} is the channel width and B_w is the vertical wall (fin) thickness. Besides, the channel width of the downstream section is related to the channel width of the upstream section as follows:

$$B_{ch,upstream} = 2 \cdot B_{ch,downstream} + B_w \tag{2}$$

The fins separating two adjacent channels have a thickness B_w equal to $B_{ch,2}$ ($a_2=1$), a choice dictated by manufacturing constraints and this is kept constant through the entire length of the heat sink. It should be noted that the authors have already developed a methodology presented in a different study [18] for obtaining the optimal dimensions (optimal a) of plate-fin heat sink channels under given constraints. However, for the purposes of the present study the simple choice of $a_2=1$ is sufficient. Consequently, the channel width in the upstream section $B_{ch,1}$ is equal to three times the width of the downstream section $B_{ch,2}$. The total channel height H_{ch} is selected as the maximum structurally possible value for thermal performance purposes [18] and it is kept constant, resulting in channel aspect ratios equal to $AR=2$ and $AR=6$ for the upstream and downstream sections respectively. Considering these geometrical parameters and by using Eqs. (1) and (2), the total number of channels results equal to six and twelve for the first and second sections of the heat sink configuration respectively. The total height of the heat sink exceeds the channel height H_{ch} by the substrate thickness t_s taken equal to the minimum feasible one achieved by using conventional machining techniques.

3. Three-dimensional numerical model formulation

The three-dimensional flow and conjugate heat transfer inside the heat sink was investigated by means of a numerical model. The overall modeling procedure and the determination of the physical and numerical parameters employed are discussed in the following paragraphs.

3.1 Flow configuration

A three-dimensional numerical model that represents the flow inside the stepwise variable-width heat sink was developed. Since modeling the entire heat sink is computationally expensive, only the periodic unit cell depicted in Fig. 2 was considered, taking advantage of the existing symmetry. Chiang et al. [19] have demonstrated that, in the case of sudden contraction flows in perfectly symmetrical domains, critical values of the aspect ratio ($H_{ch}/B_{ch,1}$), contraction ratio ($B_{ch,1}/B_{ch,2}$) and Reynolds number exist, which lead to the onset of non-symmetrical flow features. The Reynolds number values arising from the flow conditions of the present study are sub-critical (as will be shown on a later section) and thus symmetrical flow should be expected. As shown in Fig.2, the computational domain consists of a fluid and a solid sub-domain, respectively. Half the cross-section of the first-section channel and the entire cross-section of the second-section channel comprise the fluid domain, while the solid domain is composed by the vertical fins (of half thickness) and the plate substrate. Heat transfer inside the unit cell constitutes a conjugate problem as both heat conduction and convection occur in the solid and the fluid domain, respectively.

The heat sink material that was selected for the present analysis is aluminum due to its high thermal conductivity (k_{al} *=237 W/mK*) and corrosion endurance. Water was chosen as the cooling fluid with thermophysical properties (μ,ρ) regarded as constant and evaluated at the temperature of 298 K.

3.2 The governing transport equations

The heat transfer process inside the heat sink is modeled using the three-dimensional Navier-Stokes and energy equations. The equations are simplified according to the following assumptions [19,20].

(1) steady fluid flow, incompressible fluid,
(2) laminar flow,
(3) negligible viscous dissipation and radiative heat transfer
(4) negligible natural convective heat transfer

Based on these assumptions, the governing equations reduce to:

(continuity) $$\nabla \cdot \left(\rho \vec{V}\right) = 0 \tag{3}$$

(momentum) $$\vec{V} \cdot \nabla\left(\rho \vec{V}\right) = -\nabla p + \nabla\left(\mu \nabla \vec{V}\right) \tag{4}$$

(energy- fluid) $$\vec{V} \cdot \nabla\left(\rho c_p T\right) = \nabla\left(k_f \nabla T\right) \tag{5a}$$

(energy- solid) $$\nabla\left(k_s \nabla T_s\right) = 0 \tag{5b}$$

The appropriate hydrodynamic and thermal boundary conditions for the governing equations are imposed in accordance to the real operating conditions of the heat sink. A uniform velocity profile is imposed at the inlet:

$$z = 0, \qquad w = w_i,\ u = 0,\ v = 0 \tag{6}$$

while the average static pressure is taken equal to zero at the channel outlet:

$$z = L, \qquad p_{ave} = 0 \tag{7}$$

A no-slip boundary condition ($u=v=w=0$) is imposed along the fluid-wall interfaces:

$$\begin{aligned}
&x = \frac{B_w}{2} \quad for \quad y > t_s \quad \& \quad all \quad z, \quad x = \frac{B_w}{2} + B_{ch,2} \quad for \quad y > t_s \quad \& \quad z > 0.25 \\
&\frac{B_w}{2} + B_{ch,2} \le x \le B_w + B_{ch,2} \quad for \quad y > t_s \quad \& \quad z = 0.25 \\
&y = t_s \quad for \quad \frac{B_w}{2} \le x \le \frac{B_w + B_{ch,1}}{2} \quad \& \quad z < 0.25, \quad \frac{B_w}{2} \le x \le \frac{B_w}{2} + B_{ch,2} \quad \& \quad z \ge 0.25 \\
&y = H \quad for \quad \frac{B_w}{2} \le x \le \frac{B_w + B_{ch,1}}{2} \quad \& \quad z < 0.25, \quad \frac{B_w}{2} \le x \le \frac{B_w}{2} + B_{ch,2} \quad \& \quad z \ge 0.25
\end{aligned} \tag{8}$$

A symmetry boundary condition (or adiabatic wall in the case of heat transfer) is applied on both the outer vertical planes of the domain. Besides, all the outer surfaces of the domain, apart from the bottom side, are treated as adiabatic (Fig. 2):

$$\left.\begin{aligned} &x = 0 \\ &x = \frac{W_w + W_{ch,1}}{2} \\ &z = 0 \\ &z = L \\ &y = H \end{aligned}\right\} - k_s \frac{\partial T_w}{\partial n} = 0 \tag{9}$$

At the bottom surface of the computational domain, a constant heat flux is applied:

$$y = 0, \qquad -k_s \frac{\partial T_w}{\partial y} = q'' \tag{10}$$

The fluid temperature at the inlet has a specified value, while at the outlet a constant gradient is imposed:

$$z = 0, \qquad T_f = T_i \tag{11}$$

$$z = L, \qquad \frac{\partial^2 T_f}{\partial z^2} = 0 \tag{12}$$

Finally, at the solid- fluid interface, continuity of both temperature and heat flux is imposed:

$$T_w\big|_{int} = T_f\big|_{int} \tag{13}$$

$$-k_s \left.\frac{\partial T_w}{\partial n}\right|_{int} = -k_f \left.\frac{\partial T_f}{\partial n}\right|_{int} \quad (14)$$

The set of governing equations along with the boundary conditions are solved using the finite volume-based CFD package ANSYS CFX (v.13) [21]. A convergence criterion of 10^{-6} is set for the root mean square (RMS) mass, momentum and energy residuals. False transient time-stepping is used for the control of convergence, instead of explicit under-relaxation [21]. Thus, a proper physical time scale equal to the 20% of the fluid residence time inside the heat sink is selected in order to ensure convergence.

3.3 Reliability of the developed numerical model

It is essential to evaluate the reliability of the computational code in order to confirm the accuracy of the results obtained. Experimental results in configurations that are closely related to the present one could not be found, therefore suitable numerical solutions were sought instead. Barbosa-Saldaña et al. [11] investigated the three-dimensional confined laminar flow over a forward-facing step, which is a configuration that exhibits the closest resemblance to the unit cell of the present work. Therefore, for validation purposes, the dimensions of the unit cell and the boundary conditions are adjusted, as a no-slip condition (wall) is placed at the base upstream of the step instead of a symmetry boundary, so as to match the corresponding configuration found in [11]. Fig. 3a indicates the flow configuration, as also the nomenclature used in [11]. The step height s is taken equal to half the channel height H ($H=2s$) and the step is placed at a distance $l=20s$ downstream of the channel inlet, while the channel total length L and width W are $L=60s$ and $W=4s$, respectively. The Reynolds number Re_{st} that characterizes the flow is equal to 800 based on the step height and the numerical grid consists of 320000 cells. Axial velocity profiles are compared to published values at three representative positions, namely immediately upstream of the step ($X/s=19.09$), downstream of the step tip ($X/s=20.08$) and at the channel outlet ($X/s=60$). The streamwise velocity profiles along the Y direction in the middle of the channel spanwise direction are in very good agreement with the respective values of [11], as shown in Fig. 3. A small recirculation region is detected slightly upstream of the step base, where the axial velocity obtains negative values (Fig.3b), while an additional recirculation bubble of greater magnitude is evident downstream of the step leading edge, as depicted in Fig. 3c. Both regions of flow separation, which are distinct features of the flow over a forward-facing step [3], are well captured qualitatively and quantitatively. Finally, the flow obtains a parabolic profile, Fig.3d, which has not reached full development at the channel outlet.

4. Discussion of the numerical results

The numerically produced results for the variable-width configuration are presented and discussed in the following sections. The three-dimensional fluid flow inside the heat sink was critically investigated in order to point out the effects of the flow contraction on the topology of the emerging flow patterns for a wide range of Reynolds numbers within the laminar region. Subsequently, the forced convection problem is also analyzed and the effect of the secondary flow on the heat transfer performance is quantified by means of the local Nusselt number distribution.

4.1 Grid independency

A structured hexahedral grid was used for the discretization of the computational domain, with a non-uniform arrangement along the flow direction, as smaller control volumes were placed in the vicinity of the geometry constriction, in order to fully resolve the complex phenomena that occur in that region. On the other hand, a uniform grid arrangement was employed across the domain cross-section. A grid-independency analysis was conducted to verify that grid density did not affect the derived solution for the three Reynolds numbers investigated (Re=519,1038,1557).

Regarding the fluid domain, grids of increasing density (coarse-intermediate-dense) were selected, with 0.8, 2.1 and 2.5 x 10^6 cells, respectively. The horizontal axial velocity profiles at the channel mid-height at locations in the vicinity of the contraction were chosen as suitable measures to quantify the discrepancies between the different grids. As depicted in Fig. 4, the effect of the contraction on the streamwise velocity profile at an upstream to the step position is well captured by all three grids for all the Reynolds numbers considered. However, at downstream locations the velocity profile is not adequately captured by the coarse grid even for the lowest Reynolds number case (Fig. 4a). On the other hand, the intermediate grid can accurately represent the flow features for Re=519 and Re=1038, as further grid refinement produces almost identical velocity profiles for both cases. For example, the discrepancy observed between the maximum velocity values produced by the intermediate and the dense grid for Re=1038 is below 0.8%. For Re=1557 (Fig. 4c), a slightly larger discrepancy of 1.5% is observed between the maximum velocity values, despite the fact that the profiles produced by the two grids are in qualitative agreement. Therefore the intermediate grid was selected for the production of results for Re=519 and 1038, while the dense grid was used for the case of Re=1557. A grid of 1.5 x 10^6 cells was initially tested for the discretization of the solid domain at Re=1557. A grid refinement to 2.3 x 10^6 cells produced an identical value of the bottom wall mean temperature, as the discrepancy between the values produced by the two grids was below 0.1%. Consequently, the initial grid was selected as adequate for the production of results in all cases.

4.2 Topology of the emerging vortical structures

The numerical results presented in this paragraph focus on the three-dimensional features of the flow in the unit cell. The cooling fluid flow-rate $\dot{V}_{tot}$ is considered fixed and equal to 30 ml/s for the base case analyzed in this section. This flow-rate value was selected considering the applicability of the proposed heat sink design to concentrating solar applications [18]. The Reynolds number that characterizes the flow is defined using the hydraulic diameter of the channel cross section *i, i=1,2,* as the characteristic length, whilst the mean axial flow velocity inside the channels and the total volumetric flow rate are related by

$$w_{m,i} = \frac{\left(\dot{V}_{tot} \middle/ N_i \right)}{A_{ch,cs,i}} \tag{15}$$

where N_i is the number of channels in each section and $A_{ch,cs,i}$ is the channel cross-sectional area. Given that a stepwise reduction in the channel hydraulic diameter

occurs in the middle of the heat sink, two different Reynolds numbers arise as characteristics of the individual sections equal to $Re_1=519$ and $Re_2=333$ respectively, with both values lying well within the laminar region.

In order to facilitate the interpretation of the presented results, the coordinates have been properly non-dimensionalized as X^* (horizontal direction), Y^* (vertical direction), Z^* (streamwise direction) using respective characteristic lengths in each direction, so that the flow cross section is characterized by $0 \leq X^* \leq 1$ (after contraction) and $0 \leq Y^* \leq 1$, while $Z^*<0$ denotes upstream and $Z^*>0$ downstream locations of flow contraction respectively. The streamwise velocity distributions in the upstream (larger D_h) and the downstream (smaller D_h) sections of the heat sink, on the vertical channel center planes ($X^*=1.5$ and $X^*=0.5$ respectively) is presented in Fig. 5. The flow velocity in the first section upstream of the contraction (channel aspect ratio of 2) develops from one of uniform distribution ($Z^* \cong -26.042$) into a parabolic profile (Fig. 5a), which does not reach full development until the location of the contraction. The velocity profile at $Z^*=-0.52$ appears similar to the one at $Z^*= -5.21$, due to the influence of the flow contraction which causes flow deceleration. On the other hand a fully developed velocity profile is formed at a distance of $Z^* \cong 15.63$ downstream of the contraction (Fig. 5b). It is evident that the flow in the second section does not exhibit a parabolic profile but rather an almost flat fully developed velocity profile (on the Y-Z plane), due to the higher aspect ratio of the channel (channel aspect ratio of 6). The fully developed profile obtained in the second section was compared against the analytical prediction given in [22] for the same aspect ratio and excellent agreement is found. This agreement indicates that by that distance ($Z^*>15.63$), the three dimensional effects have become small and localized in the near wall regions.

Vector plots on cross-flow and horizontal planes are created in the vicinity of the contraction, in order to point out the impact this has on the upstream velocity field (Fig. 6). As seen from Fig. 6, the flow approaching the contraction branches symmetrically into two directions along the Y axis and the oncoming fluid is pushed towards the endwalls and the opposite duct corners; furthermore, the flow distribution on the horizontal (XZ) plane near the bottom wall, Fig. 6, reveals the presence of flow reversal in the endwall regions, due to the upstream deflection of the downwards moving fluid after the impingement on the respective endwall.

The inset of Fig. 7a presents the distribution of the pressure coefficient C_p on the symmetry plane of the upstream channel ($X^*=1.5$). The streamwise positive pressure gradient causes a strong deceleration of the flow and leads to final separation upstream of the contraction, whilst the negative pressure gradient in the vertical direction pushes the flow towards the endwalls. The fluid whirling motion, Fig. 7a, which is created at the end wall regions upstream of the flow contraction, develops into X-direction-oriented vortices towards the vertical channel sidewall ($X^*=0$) and thus two counter-rotating vortices near the upper and lower walls of the channel are created. These are found to increase in strength, being continuously fed by the sideways deflected fluid. The vortices obtain maximum strength at the step location, where they are deflected into the longitudinal vortices V1-V2 (Fig. 7b) over the contraction (horseshoe type of vortices). Subsequently, downstream of the contraction the vortices decrease in strength and increase in size. The flow interaction with both the fin leading surface and the endwalls is an essential condition for the onset of the symmetrical horseshoe vortices flowing on both sides of the flow-contracting fin [23,24]. The three-dimensional topology of the horseshoe vortex is shown in the detailed view of Fig. 7c, illustrating that the spiraling motion of the upstream

boundary layer becomes more intense as the channel symmetry plane (X^*=1.5) is approached.

The topology and magnitude of the secondary flow in the contraction region can be visualized even more clearly with the help of iso-surfaces of constant ω_x and ω_z vorticity, as presented in Fig. 8. As can be seen, the symmetric vortex structure onsets at the intersections of the fin leading surface and the endwalls, as illustrated by the regions of high ω_x vorticity depicted in Fig. 8a. The structure is then transformed over the contraction to a pair of ω_z vortices which persist for a significant distance downstream of the contraction before breaking down (Fig. 8b). The presence of another vortical structure of considerable magnitude close to the flow-contracting fin sidewall is detected in Figs. 7b and 8b. However, these regions of high vorticity reduce in size further downstream due to the expansion of the horseshoe vortices. It must be pointed out that such a kind of vortices have been observed by Yanaoka et al. [14] in their numerical investigation of confined flow around a blunt plate. This coherent pattern attached to the fin sidewall (V3-V4 in Fig. 7b) emerges due to the effect of the endwalls on the form of the downstream recirculation bubble, as illustrated by the iso-surface of the total vorticity depicted in Fig. 8c. The bubble appears distorted as the endwalls are approached and vortices V3-V4 are in fact the extremities of the same vortical structure. The source for the creation of this hairpin type of vortex is the parabolic flow reattachment on the fin sidewall [14].

It is thus of interest to investigate the flow patterns that arise transversely to the channel side walls, where, even in the case of two-dimensional flow [5,6], a characteristic recirculation region is clearly expected immediately downstream of the contraction. Fig. 9a presents streamwise velocity contours at different horizontal (XZ) planes in the vicinity of the geometry contraction, while Fig. 9b shows the velocity profiles along the spanwise direction (X^*) at the channel mid-height (Y^*=0.5) at three different streamwise positions: within the recirculation region (Z^*=0.10-0.25) and after the flow reattachment (Z^*=0.50) respectively. The three-dimensional nature of the flow is yet again evident as the separation bubble on each plane is of different size and it is also established that the recirculation bubble is symmetrical to the channel mid-height plane (not shown). Besides, the size of the recirculation is relatively small, as the non-dimensional reattachment length $L^*_{Z,r}$ (defined as the streamwise distance from the contraction at which the wall shear stress τ_w vanishes) at the channel mid-height is found equal to 1.14. The small value of the reattachment length is attributed primarily to the low Reynolds number (based on the fin thickness B_w [14]) which is found equal to 130. The reattachment-length value obtained by the present numerical calculations is also smaller than the experimental and numerical values for flow around a blunt plate at the same Reynolds number published by Ota et al. [25] and Yanaoka et al. [14] respectively. This is justified due to the high blockage ratio of the present study (*BR=0.33*) which tends to reduce the recirculation bubble size and has an overall stabilizing effect on the flow [12].

The topology and magnitude of the entire secondary flow pattern has a crucial impact on the performance of the heat sink. It is therefore of use to further analyze the interaction between the longitudinal vortices and the recirculation bubble that forms downstream of the fin edge. It is shown in Fig. 9a that the bubble tends to reduce in streamwise length as the endwalls are approached. In fact, it disappears completely for Y^* values larger than 0.82 (and respectively lower than 0.18). Fig. 10 elucidates the fact that the coherence of the bubble near the endwalls is destroyed due to the presence of the longitudinal vortices in that region. The action of these vortices is to bring high momentum fluid from the fluid-core region to the fin vertical wall, thus

affecting the topology of the bubble. The longitudinal vortices are visualized using vorticity iso-surfaces, while streamlines are used in order to depict the downstream recirculation. As it can be seen, the maximum dimensions of the downstream recirculation bubble extend up to locations (along the Y axis) not influenced by the presence of the longitudinal vortices. Beyond these locations, the bubble breaks down as its energy is extracted from the vortices [13].

4.3 Effect of the Reynolds number – Parametric analysis

The flow-topology examination has been further extended to larger values of the Reynolds number –Re_1=1038 and Re_1=1557- corresponding to twice and three times the flow rate of the base case, respectively. The corresponding Reynolds number in the latter case is 390 using the fin thickness as a characteristic length scale. The experimental investigation of Baker [23] revealed that no unsteady behavior of the horseshoe vortex did arise for Reynolds number values (based on the obstacle thickness) lower than 3000. Besides, numerical results for steady laminar confined flow around fins are available in the open literature for a value of the Reynolds number (based on the fin thickness) of 400 [5,14], even for lower values of the blockage ratio. Thus, the assumption of steady and laminar flow remains valid for the entire range of the examined Reynolds numbers. However, a steady-state solution could not be attained for higher values of the Reynolds number (e.g. $1850<Re<2000$), as the steady-solver residuals exhibited a regular oscillatory pattern even for the dense grid considered, indicating non-convergence.

The objective of the present parametric investigation is twofold: to cover a wide range of the heat-sink operating flow rates and to verify that the flow remains symmetric for the examined flow conditions. In order to inspect the symmetric nature of the steady flow, a modified, extended computational domain was considered, comprising a full first-section channel divided into two by the additional fin inserted at its mid-length. It must be noted that the full domain comprised only from fluid domains and was discretized using a grid consisting of twice the elements of the fluid domains of the unit cell in each case.

Fig. 11 depicts vorticity contours on two characteristic intersecting planes, which enable the characterization of the distinct flow features, for Re_1=1557. As can be seen in Fig. 11a, the flow remains perfectly symmetrical and the vortex structures that were apparent in the base case can once again be observed (vortices V1, V2, V3 and V4 of Fig. 7b); however, the vortices have an increased magnitude which is maintained for a substantial distance downstream of the contraction. Besides, the horseshoe vortices lay closer to the duct opposite wall in comparison to the base case (Re_1=519), which indicates a more intense fluid deflection after the flow impingement on the fin frontal surface. Fig. 11b illustrates that, as the streamwise distance form the contraction increases, the downstream regions of high vorticity (vortices V3-V4) tend to completely detach from the fin sidewall and to move towards the channel center plane, whilst approaching each other. Likewise, the corner vortices (V1-V2) move towards the channel vertical center plane and tend to align with the vortices V3-V4, reducing at the same time the distance between them. The existence of symmetrical flow in the full domain validates the choice of truncating the computational domain to half the width for the investigation of the base case.

Fig. 12 presents the effect of the Reynolds number on the regions of the upstream and downstream recirculation bubbles. The minima of the pressure coefficient curves depicted in Fig. 12a correspond to the location of the upstream bubble locus [23] and

indicate that the bubble moves upstream as the Reynolds number increases. Furthermore, only the two higher values of Re_1 exhibit negative values of the C_p coefficient. This is due to the fact that the development of the recirculation leads to a local pressure drop to values lower than would have been attained without the presence of the fin, i.e. had the linear drop due to friction been extended to that location. Besides, an increase on the Reynolds number value causes an approximately linear expansion of the downstream recirculation to all three dimensions, a fact elucidated by the maximum bubble dimensions depicted in Fig. 12b for each Reynolds number value.

4.4 Heat transfer – Secondary flow effects

It is of importance from an engineering point of view to illustrate the impact of the contraction-induced recirculation pattern on the overall thermal performance of the heat-sink configuration. For this reason, forced convection conditions are considered in the present analysis, in order to rule out the emergence of buoyancy-induced secondary flow that would significantly complicate the flow field. The imposed heat flux is properly selected in each case, so that the ratio Gr/Re^2 has a value much smaller than unity. It is ensured thereby that buoyancy forces are orders of magnitude smaller than inertial forces.

It has been established that the flow remains symmetrical for the examined Reynolds numbers range and therefore the results concerning heat transfer are presented for the basic unit cell geometry (Fig.2). In addition the temperature values have been non-dimensionalized as T^*, in order to allow a straightforward comparison of the computed temperature fields for different Reynolds numbers. Fig. 13 presents the temperature field in the flow contraction region on cross-flow, Fig. 13a, and streamwise planes Fig. 13b. Fig. 13a shows the development of the channel cross-section temperature distribution near the contraction, along the flow direction. The development of thermal boundary layers along the channel base and the side wall is clearly discernible for $Z^*<0$. Downstream of the contraction ($Z^*>0$), the isotherms appear distorted at the locations of the longitudinal vortices, as warm fluid from the wall boundary layers is mixed with cold fluid from the channel core. A hot spot is evident at the "eye" of the lower vortex increasing in size downstream. This topology is not present at the symmetry position near the top wall as that endwall is adiabatic; clearly the temperature distribution on the cross stream planes is not symmetrical about the $Y^*=0.5$ plane. A closer examination of Fig. 13a also reveals fluid cooling occurring at the bottom thermal boundary layer immediately upstream of the contraction (e.g., see plot at $Z^*=-0.1$). This rather distinct temperature distribution can be explained by the presence of the reverse flow of cold fluid in the horseshoe-vortex region (Fig. 7), which gives rise to axial heat transfer in the fluid thermal boundary layers and redistribution of thermal energy.

Fig. 13b exhibits a detailed view of the temperature distribution along the flow direction, particularly in the contraction region. A sequence of overlapping warm and cold water layers is evident close to the endwalls. The formation of characteristic streaks downstream of the contraction is accounted for, considering the entrainment back to the main flow of the elements of the fluid core that form the pair of horseshoe vortices which subsequently transform to longitudinal vortices downstream of the contraction. The fact that the distorted topology of the temperature contours, Fig. 13a, coincides with the streaks observed in Fig. 13b, also clarifies the effect of the vortices on the axial temperature distribution.

Fig.14 presents contours of the wall heat flux normalized by the mean overall heat flux q_m'' on the channel bottom wall (Fig.14a) and on the fin sidewall (Fig.14b), respectively. It is evident that the local wall heat flux at the bottom wall in the vicinity of the fin base obtains much larger values in comparison to the mean heat flux inside the heat sink (Fig. 14a), which is a clear evidence that heat transfer is significantly enhanced in the region under the influence of the lower horseshoe vortex. An interesting feature that may be observed is a region of local flux reversal (heat transfer from the fluid to the heat-sink base) which develops near the channel wall immediately upstream of the contraction region. This is due to the cooling of the channel bottom wall under the action of the lower horseshoe vortex, while the fluid above and within the sidewall boundary layer maintains its elevated temperature. Although the occurrence of flux reversal is undesirable, the effect it has on heat transfer is localized and limited to a small area in the vicinity of the contraction. The effect of the horseshoe vortex on heat transfer is also illustrated by the flux distribution at the fin sidewall, Fig. 14b, as the area influenced by the action of the lower vortex exhibits high local heat flux values. It is obvious, that the lower vortex predominantly contributes to the heat transfer enhancement due to the fact that this mainly takes place on the channel bottom wall, while the upper wall is adiabatic.

The local Nusselt number distribution constitutes an illustrative way to quantify the heat transfer rate inside the heat sink under different operating conditions. As the local heat flux and temperature distributions are available from the numerical simulation, the local convective heat transfer coefficient can be determined from:

$$h(z) = \frac{q_{ave}(z)}{T_{w,ave}(z) - T_m(z)} \tag{16}$$

where $q_{ave}(z)$ and $T_{w,ave}(z)$ are the circumferentially averaged heat flux and bottom wall temperature values, respectively:

$$q_{ave}(z) = \frac{1}{P}\int_P q dl \tag{17}$$

$$T_{w,ave}(z) = \frac{1}{P}\int_P T_w dl \tag{18}$$

and P is the channel perimeter. $T_m(Z)$ is the local fluid bulk mean (mixing cup) temperature defined as:

$$T_m = \frac{1}{w_m A_{ch,cs}} \int_{A_{ch,cs}} w(x,y) T(x,y) dA_{ch,cs} \tag{19}$$

where w_m is the mean, streamwise flow velocity inside the channel. The circumferentially averaged local Nusselt number can then be derived from the relation

$$Nu_i(z) = h(z)\frac{D_{h,i}}{k_f} \tag{20}$$

where k_f is the fluid thermal conductivity and $D_{h,i}$ is the hydraulic diameter of each section, i=1,2. Fig. 15a shows the averaged local Nusselt number values along the flow direction for the three values of the Reynolds number considered. The theoretical values of the Nusselt number [22] for thermally fully developed parallel flow in channels having aspect ratios equal to the heat sink first (AR=2) and second section (AR=6), respectively, are also plotted in Fig.15 for the sake of comparison. As can be seen, close to the channel inlet and away from the contraction influence the Nusselt number distribution behaves like a typical thermal entry flow. As the contraction is approached, the distribution shows a rapid decrease in the range of axial locations $-4<Z^*<0$. Nevertheless, this decrease of the heat transfer rate is not associated with a hot spot at the surface of the channel wall, as shown in Fig. 15b. The wall temperature in fact decreases prior to the contraction due to the influence of the second section and the action of the horseshoe vortices. On the other hand, fluid boundary layers of elevated temperature have developed adjacent to the walls. As a result, the temperature gradient *dT/dy* at the solid-fluid interface is considerably decreased in the specified region and consequently the heat flux (*q"=-kdT/dy*) and the Nusselt number values also decrease. The abrupt heat transfer augmentation in the contraction region is attributed to the flow impingement on the leading surface of the emerging fin. As can be seen from the inset of Fig. 15, a second local Nusselt number maximum is observed due to the flow reattachment in the second heat sink section.

Downstream of the contraction, the Nusselt number maintains relatively constant values, which are higher than those expected for fully developed parallel flow in a channel of AR=6 [22].This further heat transfer enhancement throughout the heat sink second section is attributed to the presence of the two horseshoe vortices and especially of the one toward the channel bottom wall . The vortex constantly floods the heated bottom wall with cold fluid from the channel core causing disruption of the developing thermal boundary layer and thermal mixing. As a result, mixing zones consisting of cold and warm fluid layers emerge in the region of the boundary layer, which persist further downstream. If the channels of the first section were extended over the entire length of the heat sink and the flow remained parallel, the Nusselt number values would have gradually approached the fully developed value of 4.1. With the stepwise reduction of the channel hydraulic diameter however heat transfer is enhanced, as the aforementioned value is significantly exceeded.

A closer look at Fig. 15a reveals that the obtained Nusselt number values for Re_1=519 are higher that the respective for Re_1=1038 at axial locations of $Z^*>18$.This slightly decreased heat transfer rate (by approximately 4%) for Re_1=1038 is attributed to the three-dimensional effects and more specifically the effect of the sidewall vortex V4 on heat transfer, whereby fluid of elevated temperature is drawn from the thermal boundary layer near the bottom wall toward the channel mid-height (see Fig.7b). Thus, the thermal boundary layer of the fin sidewall in the vicinity of the channel mid-height thickens locally and heat transfer is reduced. The effect appears to be significant for the two higher values of the Reynolds number as the Nusselt number values exhibit the same trend, while, on the contrary, the values for Re_1=519 remain approximately constant. The influence of the sidewall vortex becomes more evident as thermal full development is approached and the Nusselt number tends to an asymptotic value.

4.5 Overall performance enhancement

A configuration comprising straight rectangular channels of hydraulic diameter $D_{h,2}$ is selected as a reference case, in order to evaluate the overall performance of the variable-width design. The evaluation is based on a performance index defined here as the heat transfer to pressure drop ratio [26]:

$$e = \frac{\bar{h} / \bar{h}_0}{\Delta p / \Delta p_0} \tag{21}$$

where $\bar{h}$ is the overall heat transfer coefficient and Δp is the cooling fluid pressure drop. It must be noted that the values of the straight-channel design are denoted with the subscript *0*. The results of the comparative investigation are presented in Table 1. It is evident from the values of the table that a maximum performance enhancement of 41% is obtained for Re_1=519, while the enhancement decreases for higher Re_1 numbers. As has been explained in the previous paragraph, the addition of heat transfer surfaces, assisted by the presence of the longitudinal vortices in the second half of the heat sink compensates for the moderate thermal performance of the first section. As a result, the variable-width configuration is of equivalent thermal performance to straight channel designs of reduced geometrical scale, which have an intrinsic advantage in terms of heat transfer [27]. On the other hand, the incorporation of wide channels in the heat-sink first section significantly reduces the pressure drop penalty (see Table 1) leading to a considerable enhancement of the overall performance.

Certainly, the effect of alternative geometric designs arising, for instance, by varying the length of the increased-fin-number section, would have deserved further investigation, but this would have required significant additional computational effort and was considered outside the scope of the present work. From the comparative results however, some intuitive conclusions may be drown. It can be, for instance, deduced that the extension of the second section to a length greater than L/2 would lead to further heat transfer enhancement, as channels of smaller hydraulic diameter would occupy a larger part of the heat sink, accompanied by the introduction of an additional pressure drop penalty. The limitation of the second section to a length less than L/2 would have the opposite effect. However, as the Reynolds number increases, the relative increase of the pressure drop is large and consequently the overall enhancement is reduced, a trend expected to be more profound for configurations oriented toward high thermal performance. It is therefore suggested that the heat sink be operated at moderate values of the Reynolds number, provided that adequate thermal performance is achieved for the given heating conditions.

5. Conclusions

Laminar flow inside a plate-fin heat sink with a stepwise-variation (reduction) in channel width, appropriate for dissipating high heat fluxes was numerically investigated in the present study. The flow undergoes an abrupt contraction midway across the heat sink, as the number of the cooling fluid passages is doubled. The strongly three-dimensional nature of the flow in the vicinity of and due to the step

change in channel width was manifested through the formation of two counter-rotating longitudinal vortices near the upper and lower heat-sink walls and of a coherent hairpin-like vortex near the fin sidewall region downstream of the contraction. The former set of vortices were identified as being of the horseshoe-type, as the source of their onset is the rolling up of the endwall boundary layer under the effect of an adverse pressure gradient, which develops due to the presence of the flow-contracting fin. The characteristic separation bubble formed immediately downstream of the fin leading edge exhibited a three-dimensional symmetrical form and was of reduced size in comparison to the single blunt plate case due to the effect of the high blockage ratio. In the regions under the influence of the horseshoe vortices the bubble decayed completely. The entire recirculation pattern was found to remain symmetrical and the flow was steady up to the highest Reynolds number examined.

The emerging secondary flow caused intense fluid mixing that lead to the formation of overlapping cold and warm fluid layers in a streaky pattern downstream of the contraction. The crucial impact of the longitudinal vortices on heat transfer was verified, as the local wall heat flux in regions under the influence of the horseshoe vortices was as high as 5.5 times the mean value. Besides, the minimum local Nusselt number value attained in the heat-sink second section is approximately equal to 8, which is considerably higher than the theoretically predicted value for fully developed parallel channel flow under forced convection conditions (6.05). Finally, through the comparison to a fixed-width configuration, it was demonstrated that the variable-width design exhibits superior overall performance, which is owed to two reasons: (a) the heat transfer enhancement due to the increase of the heat-transfer areas in the second heat-sink section and the formation of longitudinal vortices and (b) the pressure drop reduction due to the presence of wide channels, thus fewer friction surfaces, in the first heat-sink section.

Acknowledgments

The simulations were performed using the Cloud Computing infrastructure of the NTUA computer center. The computer center staff is gratefully acknowledged for the disposed storage space and technical support. This work was financially supported by the NTUA Special Account for Research.

References

[1] B.F. Armaly, F. Durst, J.C.F. Pereira, B. Schönung, Experimental and theoretical investigation of backward-facing step flow, J. Fluid Mech. 127 (1983) 473-496.

[2] B.F. Blackwell, B.F. Armaly, Benchmark problem definition and summary of computational results for mixed convection over a backward facing step, ASME Heat Transfer Div. (Publication) HTD 258 (1993) 1-10.

[3] S.C.R. Dennis, F.T. Smith, Steady flow through a channel with a symmetrical constriction in the form of a step, Proc. R. Soc. Lond. 372 (1980) 393-414.

[4] D.M. Hawken, P. Townsend, M.F. Webster, Numerical simulation of viscous flows in channels with a step, Comp. Fluids 20 (1991) 59-75.

[5] N. Djilali, Forced laminar convection in an array of stacked plates, Num. Heat Transfer, Part A, 25 (1994) 393-408.

[6] M. Rahnema, M.A. Yaghoubi, H. Kazeminejad, A numerical study of convective heat transfer from an array of parallel blunt plates, Int. J. Heat Fluid Flow 18 (1997) 430-436.

[7] P. Marty, F. Michel, P. Tochon, Experimental and numerical study of the heat transfer along a blunt flat plate, Int. J. Heat Mass Transfer 51 (2008) 13-23.

[8] H. Stüer, A. Gyr, W. Kinzelbach, Laminar separation on forward facing step, Eur. J. Mech. B/Fluids 18 (1999) 675-692.

[9] J.F. Largeau, V. Moriniere, Wall pressure fluctuations and topology in separated flows over a forward facing step, Exp. Fluids 42 (2007) 21-40.

[10] D. Wilhelm, C. Härtel, L. Kleiser, Computational analysis of the two-dimensional-three-dimensional transition in forward-facing step flow, J. Fluid Mech. 489 (2003) 1-27.

[11] J.G Barbosa-Saldaña, N.K. Anand, Flow over a three-dimensional horizontal forward-facing step, Num. Heat Transfer Part A 53 (2008) 1-17.

[12] M. Yaghoubi, E. Velayati, Conjugate heat transfer from surface-mounted finite blunt plates, Proc. I. Mech. Eng. Part C: J. Mech. Eng. Sci. 220 (2006) 83-94.

[13] L.W. Zhang, S. Balachandar, D.K. Tafti, Effects of intrinsic three dimensionality on heat transfer and friction loss in a periodic array of parallel plates, Num. Heat Transfer: Part A 31 (1997) 327-353.

[14] H. Yanaoka, H. Yoshikawa, T. Ota, Numerical simulation of laminar flow and heat transfer over a blunt flat plate in square channel, Trans. ASME J. Heat Transfer 124 (2002) 8-16.

[15] H. Nakamura, T. Igarashi, T. Tsutsui, Local heat transfer around a wall-mounted cube in the turbulent boundary layer, Int. J. Heat Mass Transfer 44 (2001) 3385-3395.

[16] E.R. Meinders, K. Hanjalić, Vortex structure and heat transfer in turbulent flow over a wall-mounted matrix of cubes, Int. J. Heat Mass Transfer 20 (1999) 255-267.

[17] J.Barrau, D. Chemisana, J. Rosell, L. Tadrist, M. Ibañez, An experimental study of a new hybrid jet impingement/micro-channel cooling scheme, Appl. Therm. Eng. 30 (2010) 2058-2066.

[18] I.K. Karathanassis, E. Papanicolaou, V. Belessiotis, G.C. Bergeles, Multi-objective design optimization of a micro heat sink for Concentrating Photovoltaic/Thermal (CPVT) systems using a genetic algorithm, Appl. Therm. Eng. In Press.

[19] T.P. Chiang, A. Sau, R.R. Hwang, Asymmetry and bifurcations in three-dimensional sudden-contraction channel flows, Phys. Rev. E 83 (2011) art. no. 046313.

[20] P.S. Lee, S.V. Garimella, Thermally developing flow and heat transfer in rectangular microchannels of different aspect ratios, Int. J. Heat Mass Transfer 49 (2006) 3060-3067.

[21] ANSYS Inc., ANSYS CFX-Solver theory guide, Release 13.0, Canonsburg, PA 2010.

[22] R.K. Shah, A.L. London, Laminar Flow Forced Convection in Ducts: a Source Book for Compact Heat Exchangers, Academic press, New York, 1978.

[23] C.J. Baker, The laminar horseshoe vortex, J. Fluid Mech. 95 (1979) 347-367.

[24] R.L. Simpson, Junction flows, Annu. Rev. Fluid Mech. 33 (2001) 415-443.

[25] T. Ota, Y. Asano, J. Okawa, Reattachment length and transition of the separated flow over blunt flat plates, Bull. JSME 24 (1981) 941–947.

[26] D.W. Kim, Convection and flow boiling in microgaps and porous foam coolers, PhD Thesis, University of Maryland, College Park, MD, 2007.

[27] D.B. Tuckerman, R.F.W. Pease, High-performance heat sinking for VLSI, IEEE Electron Device Letters 2 (1981) 126-129.

Tables

Table 1
Comparison between the two heat-sink designs.

	ΔP [Pa]		**e [-]**
	fixed-width	variable-width	variable-width
Re_1=519	74.3	45.4	1.41
Re_1=1038	152.7	101.6	1.33
Re_1=1557	235.1	174.9	1.22

Figures

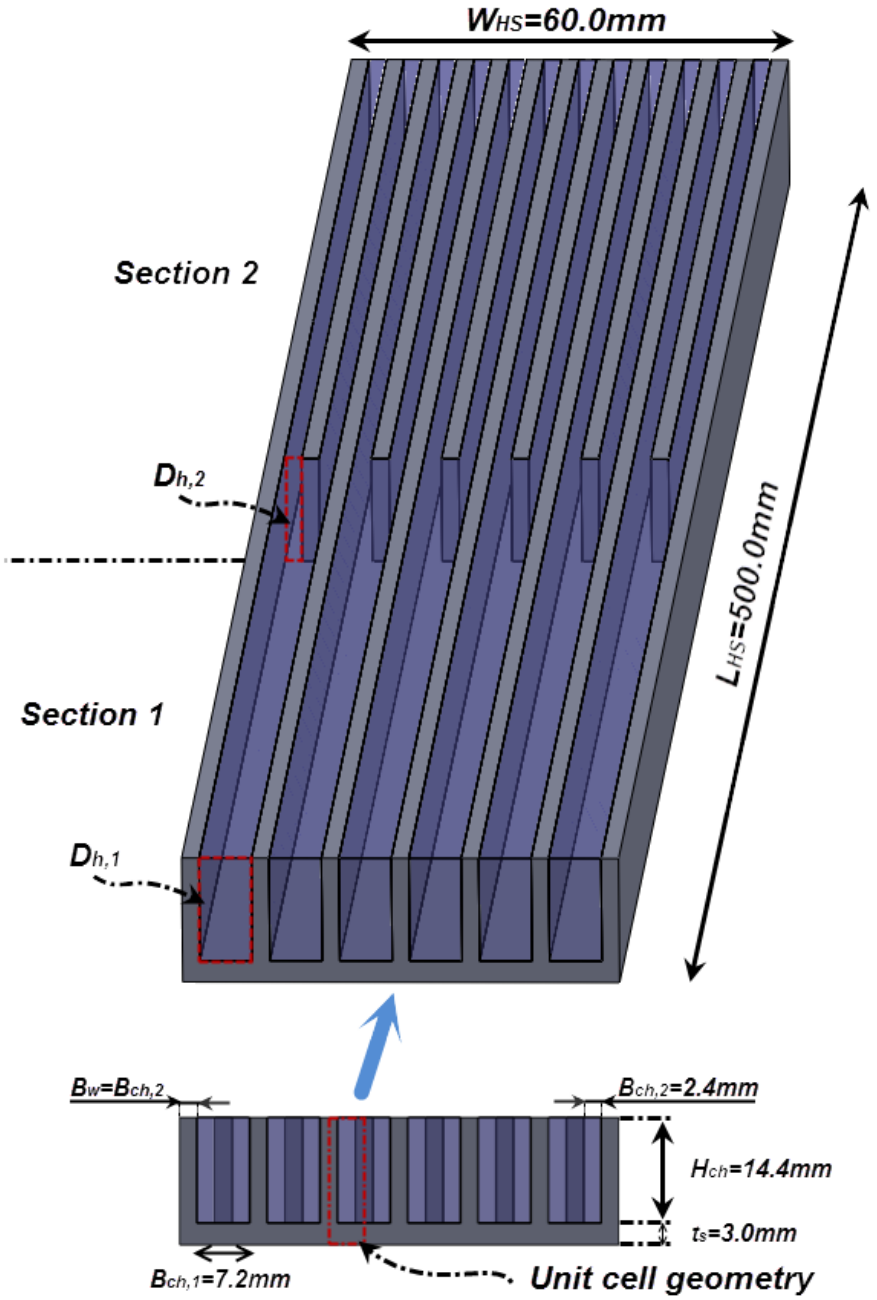

Fig. 1. Geometrical parameters of the plate-fin heat sink configuration under investigation.

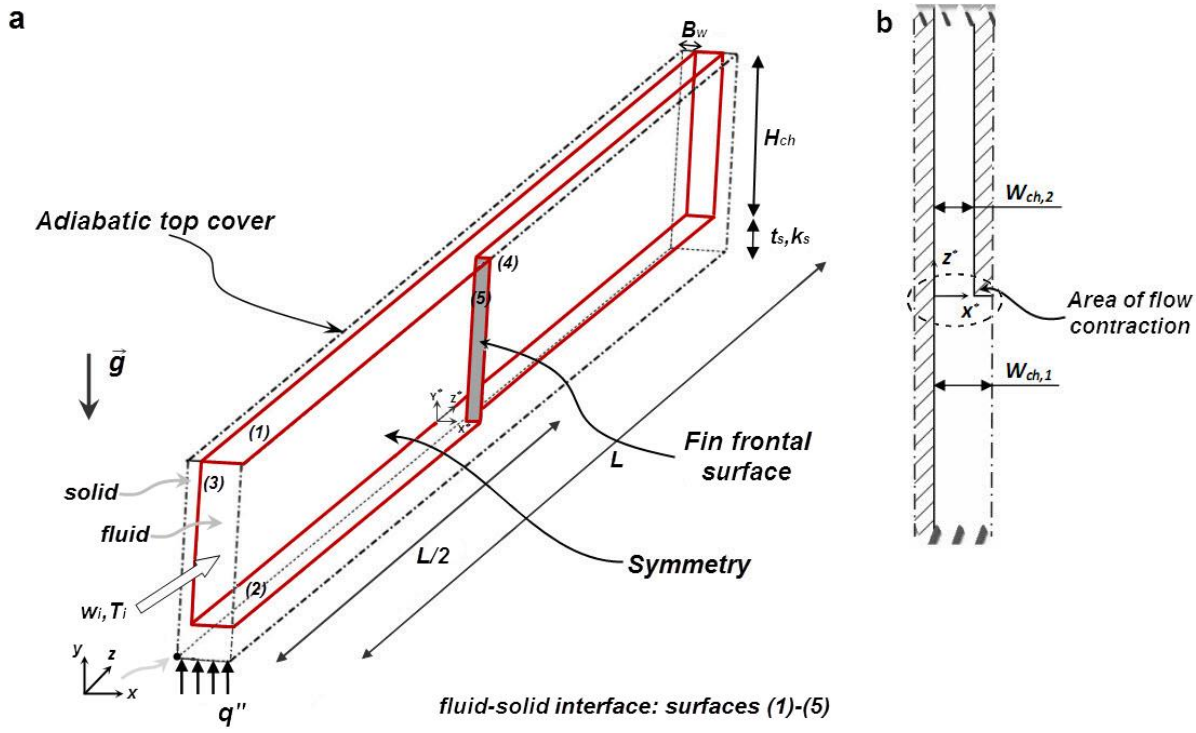

Fig. 2. Computational domain for the numerical model: (a) Perspective view, (b) horizontal cross section detail near the flow contraction.

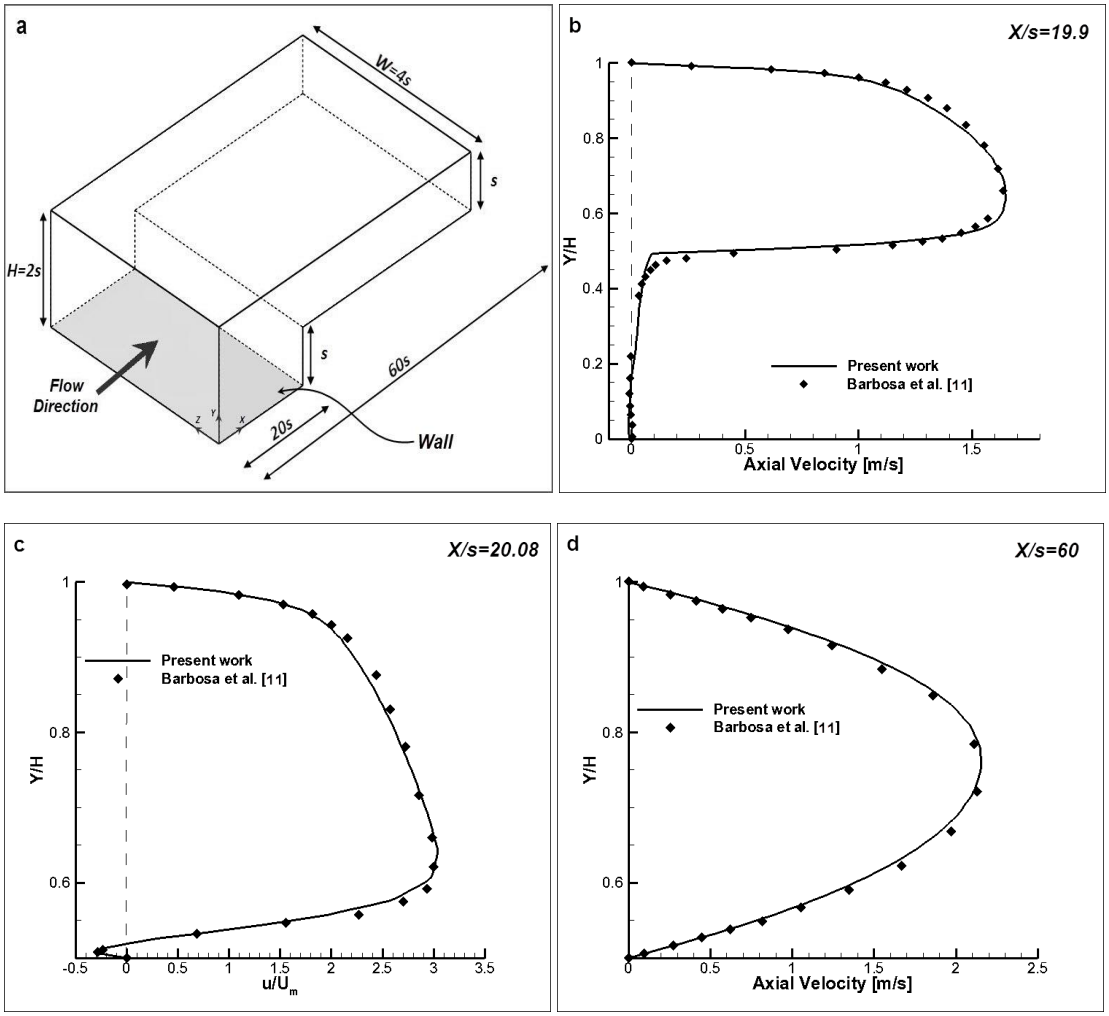

Fig. 3. Code validation for the case of Barbosa-Saldaña et al. [11]. (a) Computational domain. Vertical velocity profiles on the domain symmetry plane (Z/W=0.5) at Re_{st}=800: (b) immediately upstream of the vertical step wall, (c) downstream of the step edge (U_m=0.617 m/s) and (d) at the channel outlet.

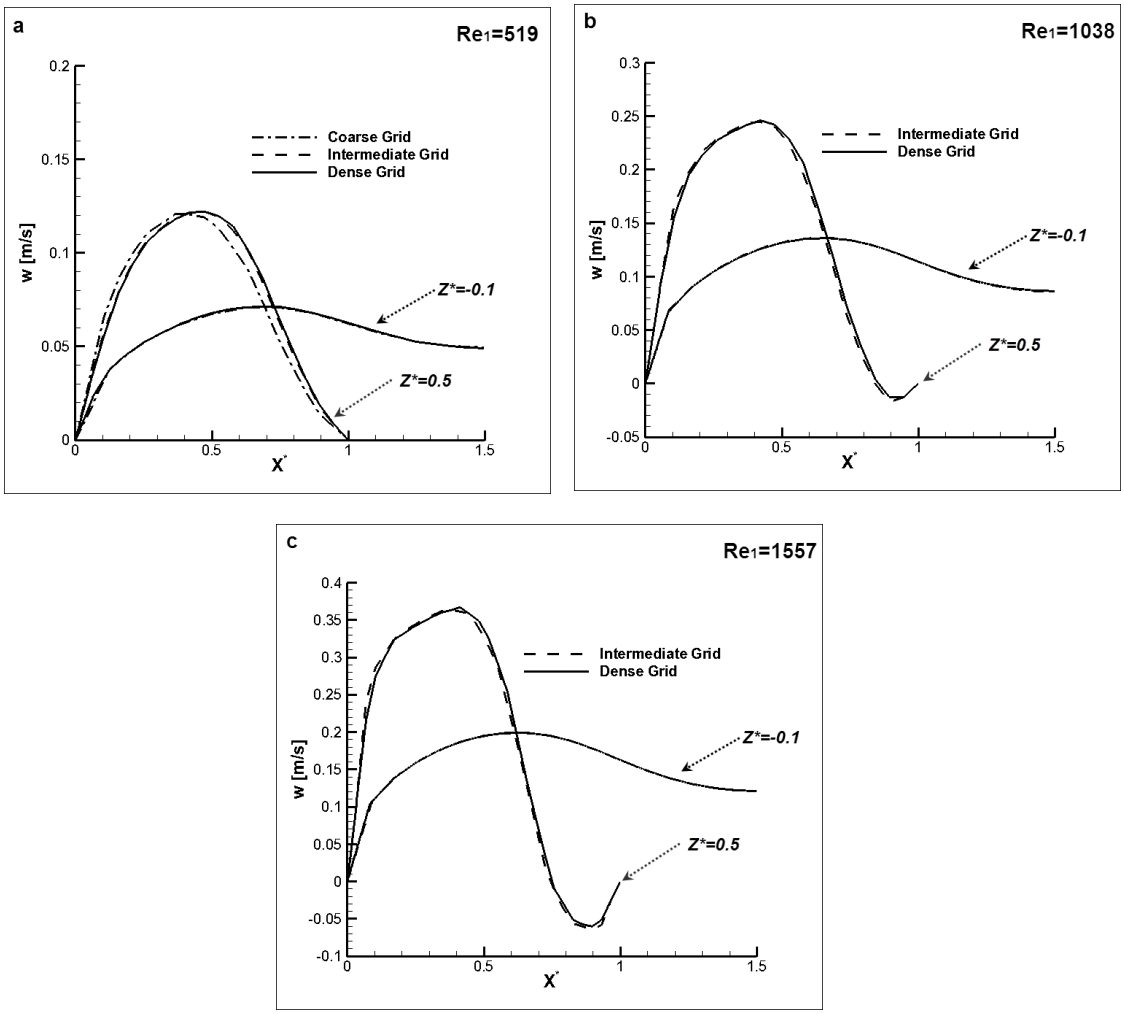

Fig. 4. Effect of grid refinement. Axial velocity profiles at the channel mid-height (Y^*=0.5): (a) Re_1=519, (b) Re_1=1038 and (c) Re_1=1557.

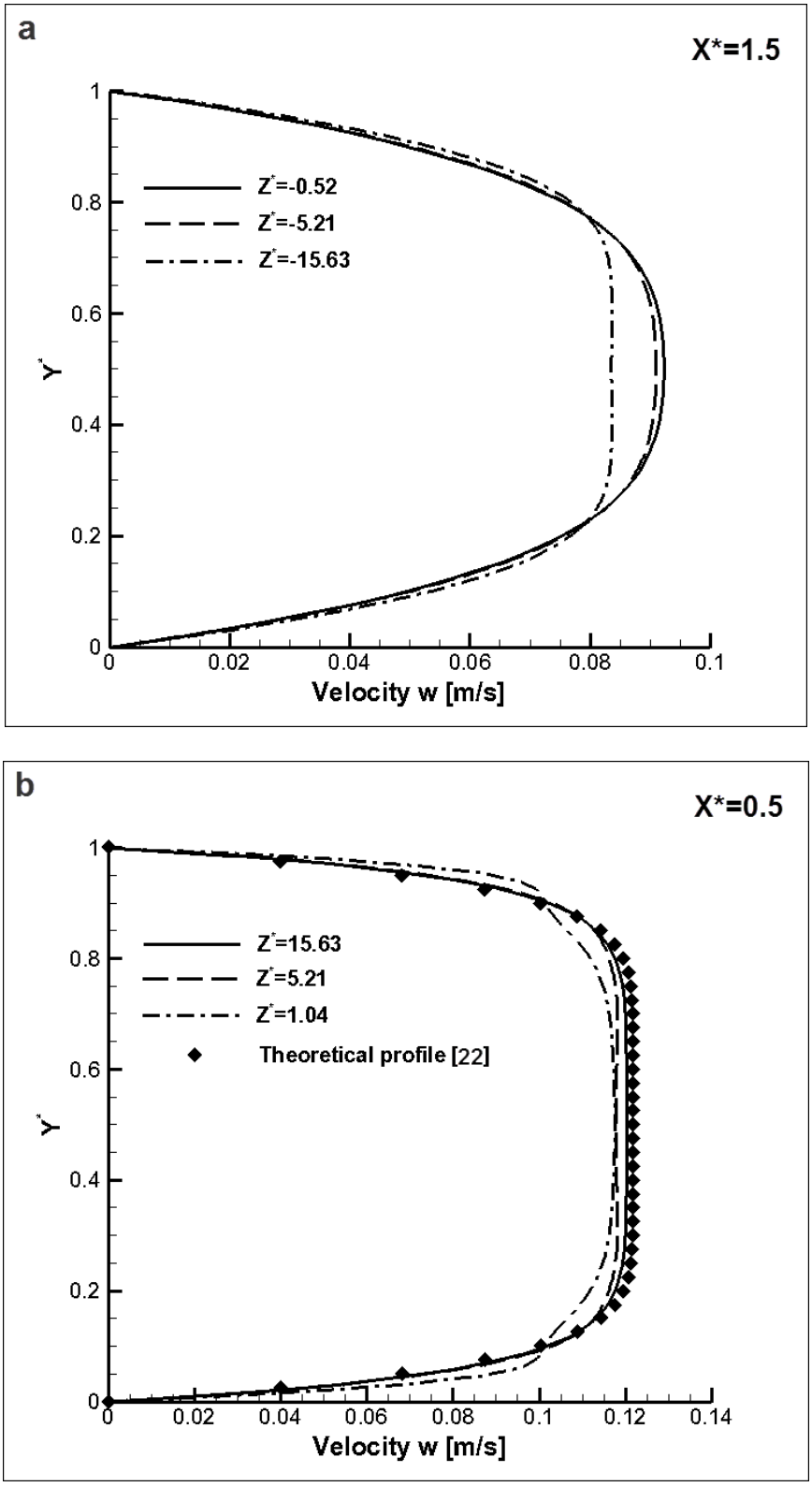

Fig. 5. Vertical profiles of w-velocity at the (a) first ($Z^*<0$) and (b) second section ($Z^*>0$) of the unit cell.

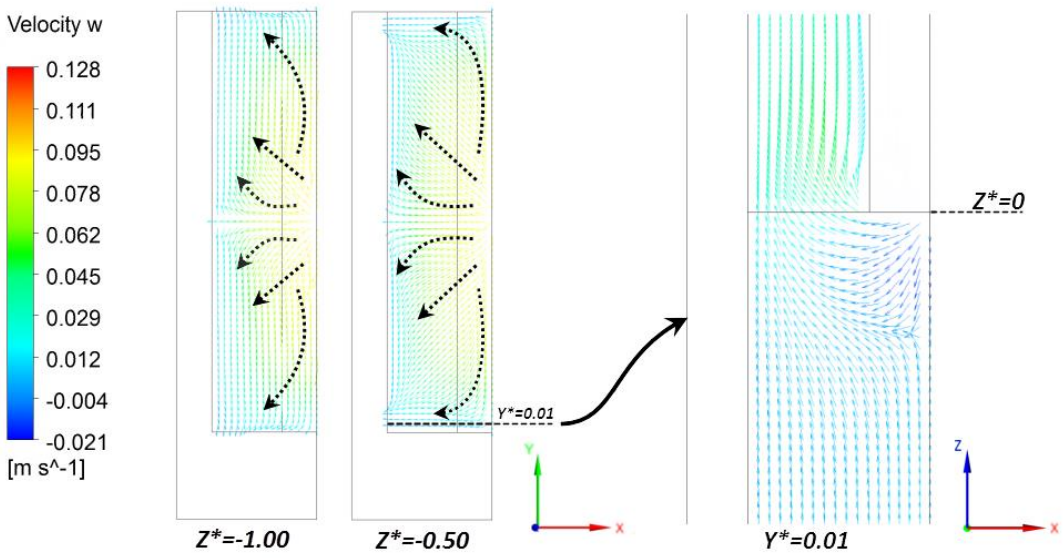

Fig. 6. Effect of the contraction on the upstream velocity field ($Z^{*}<0$) at Re_1=519.

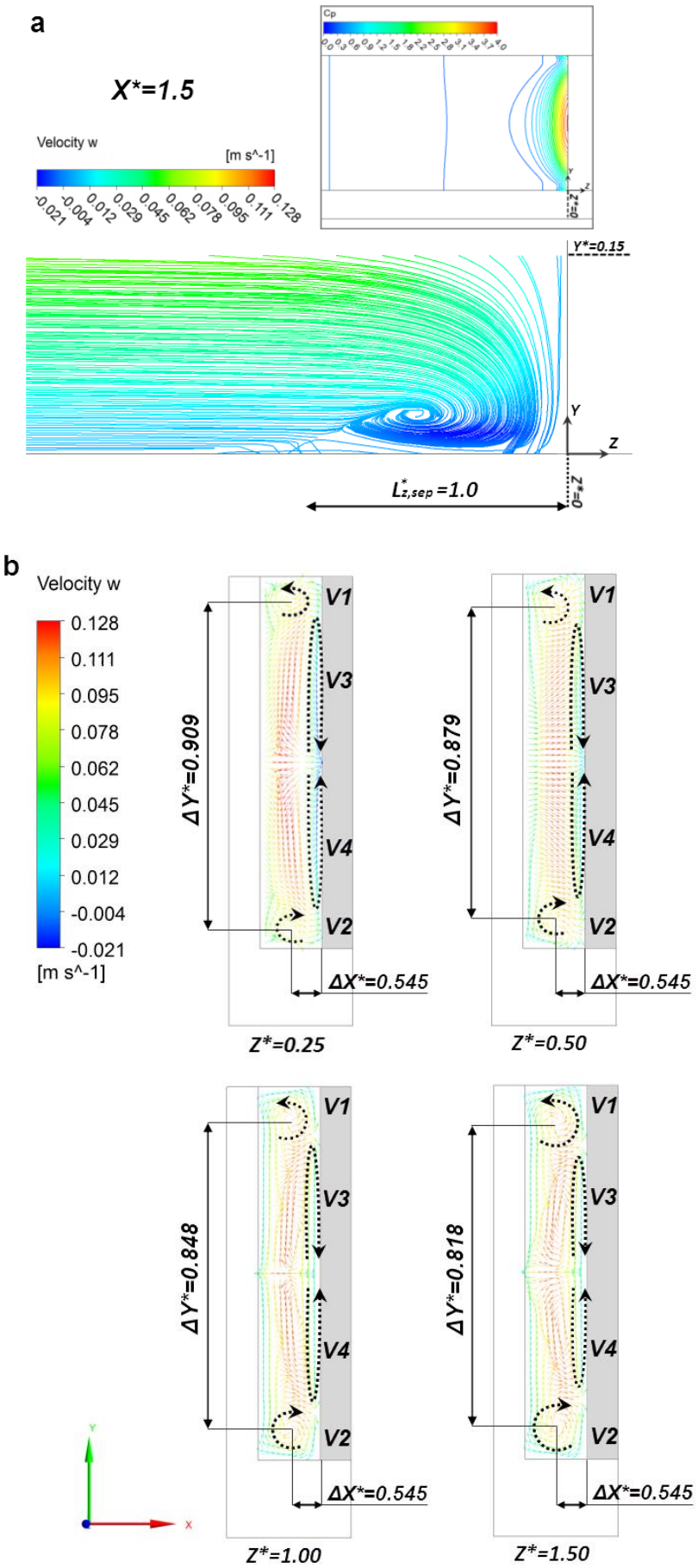
a
X*=1.5
Velocity w
[m s^-1]
-0.021
-0.004
0.012
0.029
0.045
0.062
0.078
0.095
0.111
0.128
Cp
Y*=0.15
Y
Z
Z*=0
L*z,sep =1.0
b
Velocity w
0.128
0.111
0.095
0.078
0.062
0.045
0.029
0.012
-0.004
-0.021
[m s^-1]
V1
V3
V4
V2
ΔY*=0.909
ΔX*=0.545
Z*=0.25
ΔY*=0.879
Z*=0.50
ΔY*=0.848
Z*=1.00
ΔY*=0.818
Z*=1.50

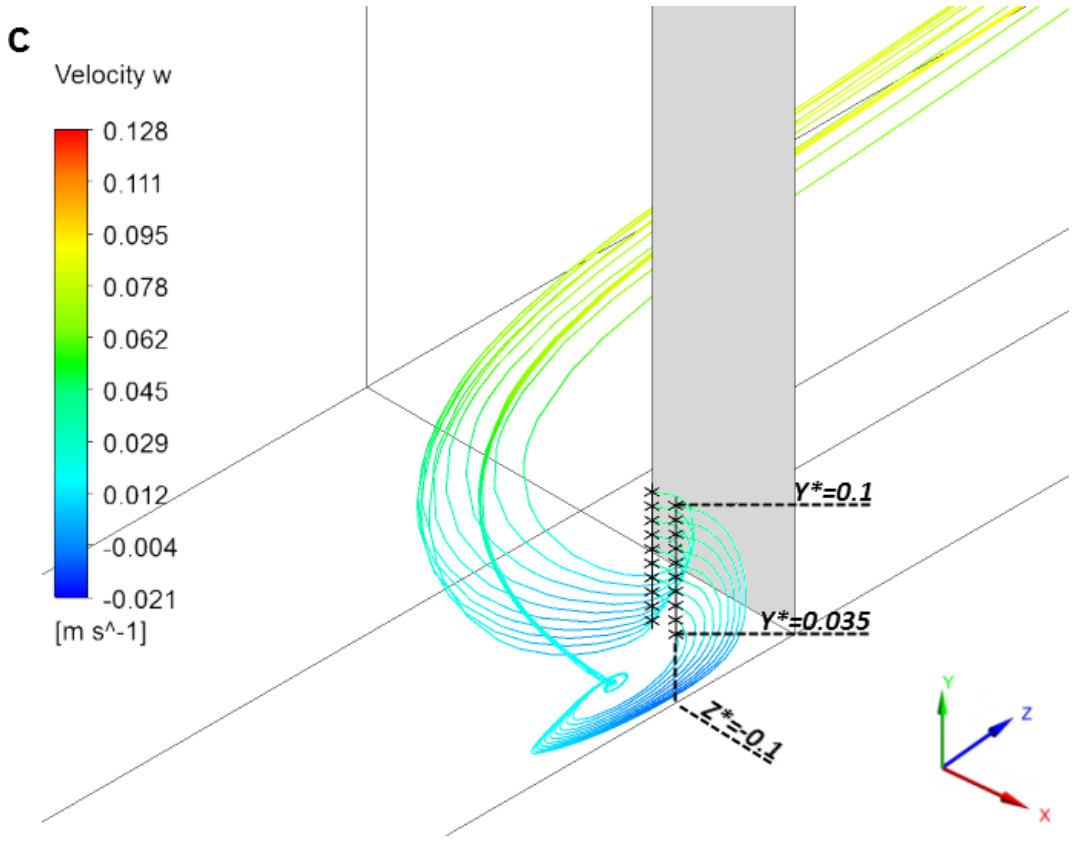

Fig. 7. Reference case (Re_1=519): (a) Rolling up of the bottom wall boundary layer. (b) Vector plots on cross-flow planes downstream of the contraction. (c) Three-dimensional streamlines originating from seed points at X^*=1.42 and X^*=1.5, respectively.

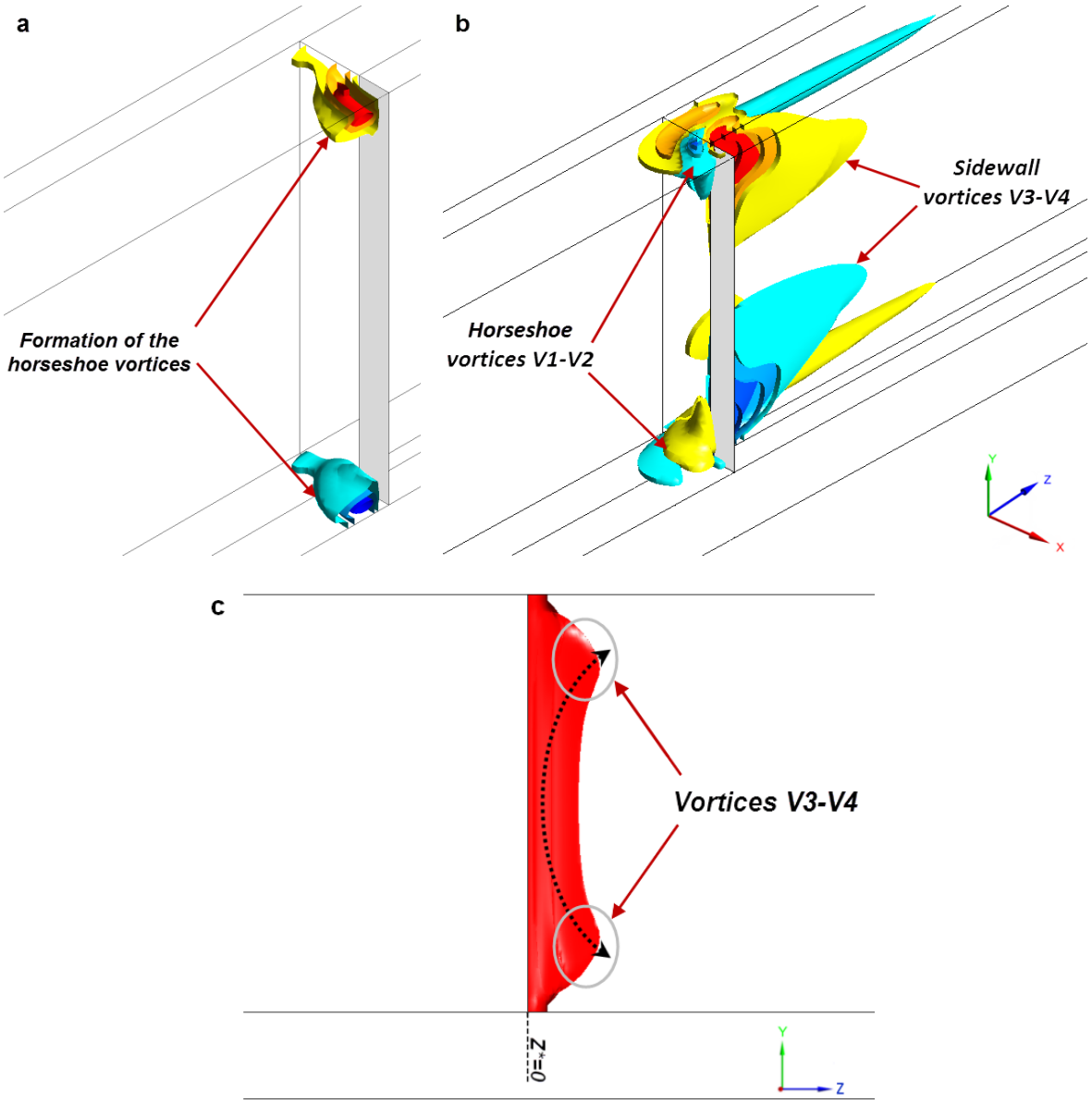

Fig. 8. Iso-surfaces of (a) the ω_x and (b) the ω_z vorticity (Re_1=519). Three pairs of surfaces of equal magnitude (ω_x=100-75-50 s^{-1}, ω_z=50 - 25 -12.5 s^{-1}) and opposite sign are presented (red-maximum vorticity, blue-minimum vorticity). (c) Iso-surface of the total vorticity $|\omega|$=200s^{-1}.

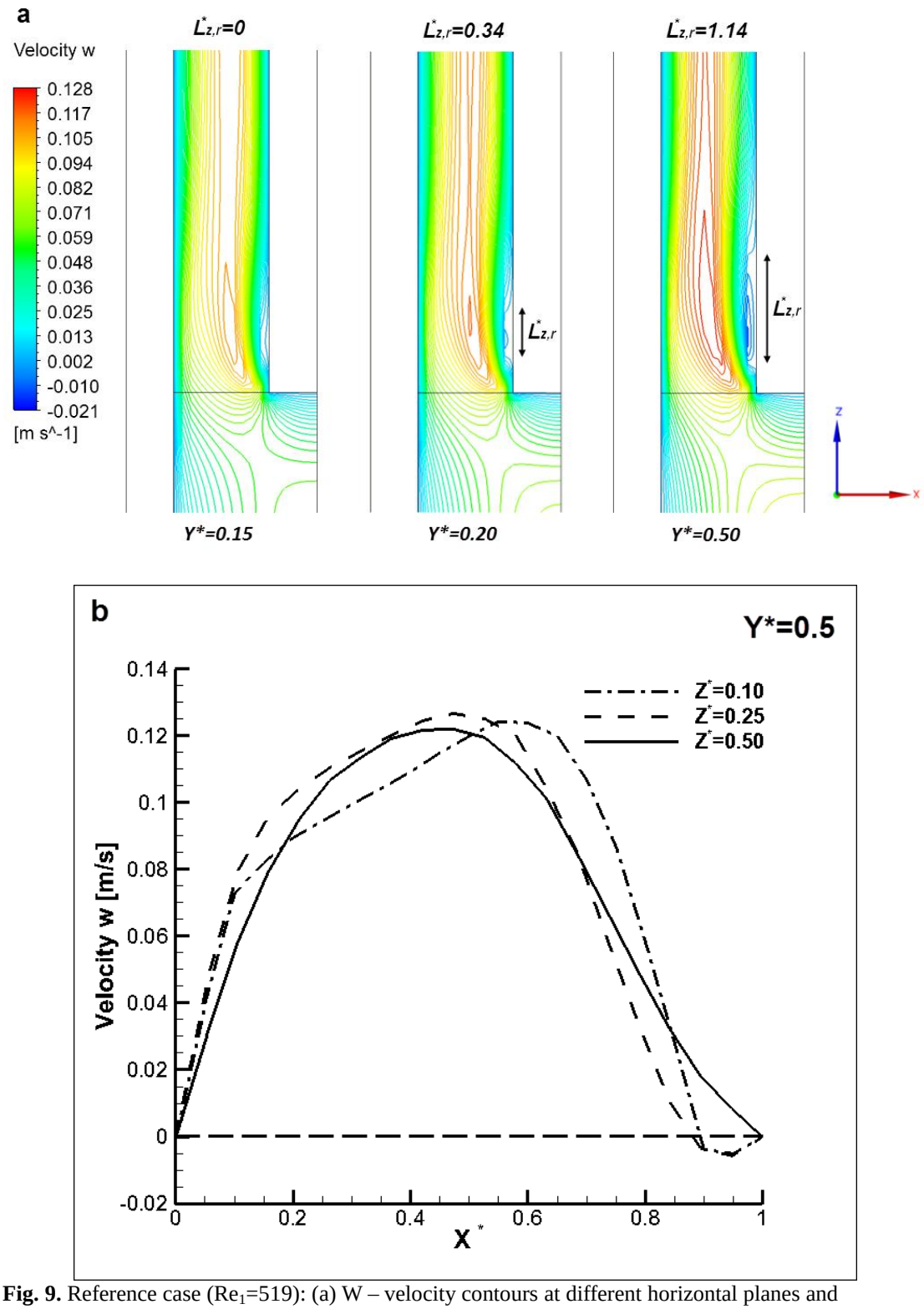

Fig. 9. Reference case (Re_1=519): (a) W – velocity contours at different horizontal planes and respective bubble lengths $L^*_{z,r}$, (b) w - velocity profiles along the spanwise direction.

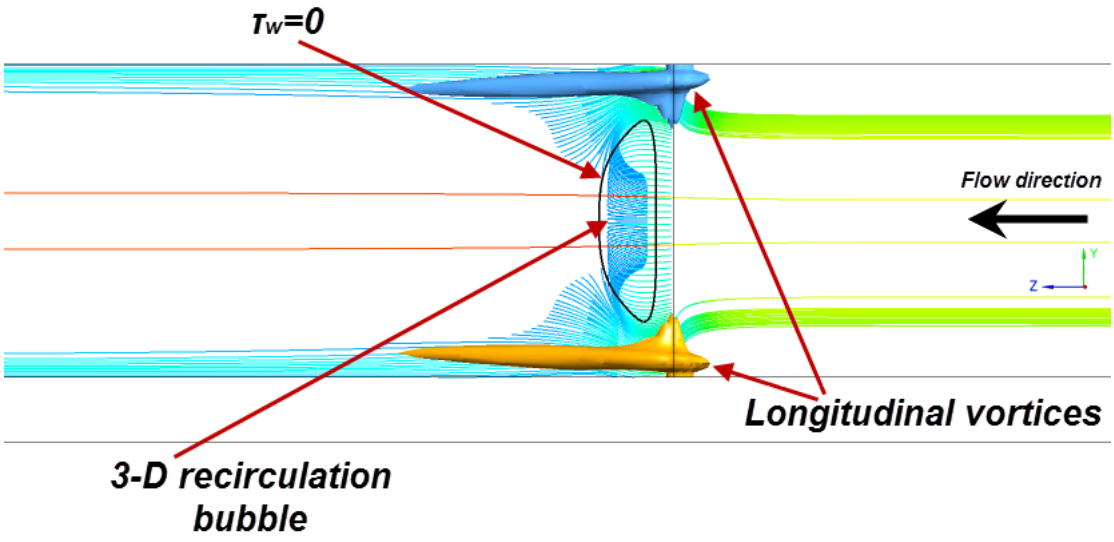

Fig. 10. Interaction of the downstream vortical structures (Re_1=519). The vortices are visualized using ω_z isosurfaces (of magnitude 12.5 s-1), while the bubble is illustrated through 3-D streamlines colored according to the axial velocity.

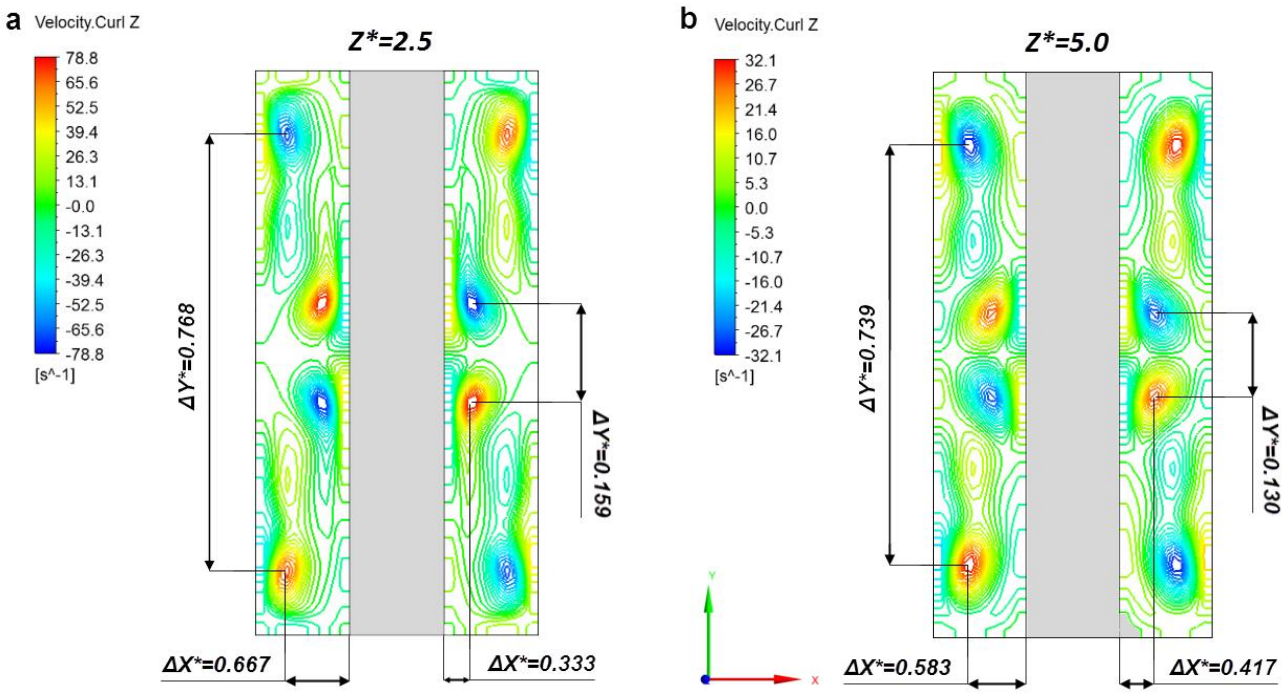

Fig. 11. Symmetry verification on an extended domain (Re_1=1557): Contour plots of the ω_z vorticity on cross-flow planes at (a) Z^*=2.5 and (b) Z^*=5.0.

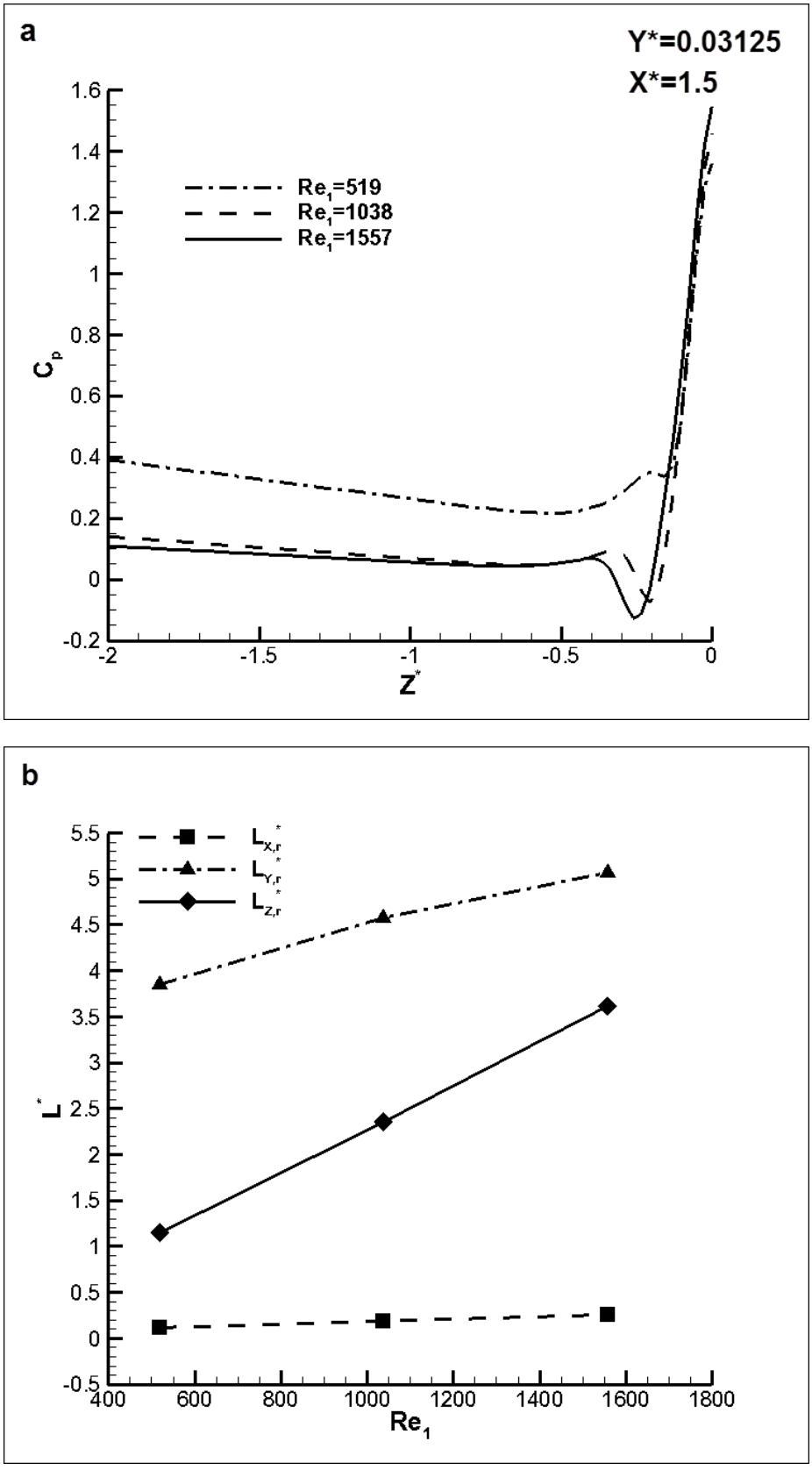

Fig. 12. (a) Upstream pressure variation in the vicinity of the lower endwall. (b) Maximum dimensions of the downstream separation bubble vs. Re_1.

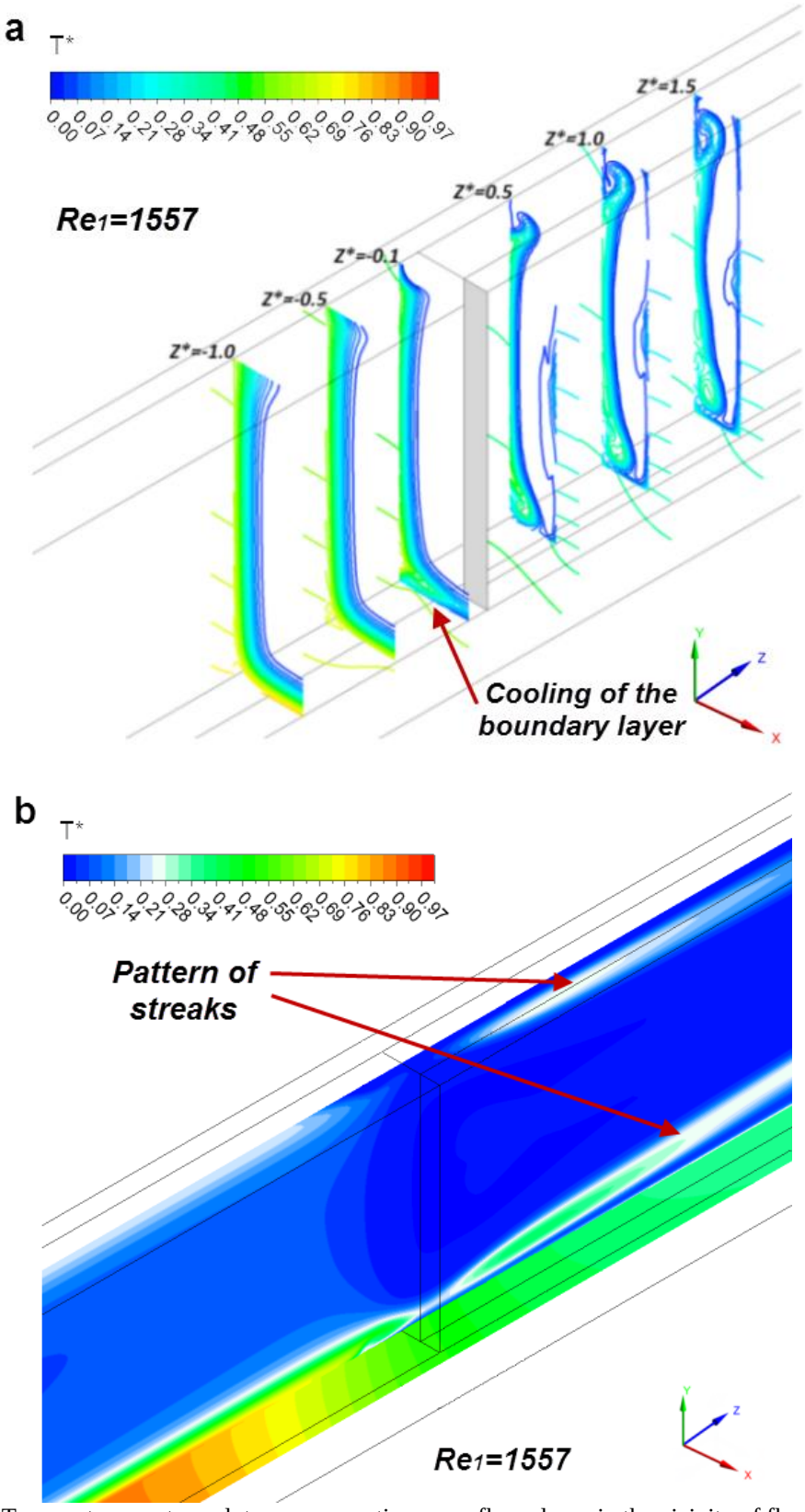

Fig. 13. (a) Temperature contour plots on consecutive cross-flow planes in the vicinity of flow contraction and (b) on a longitudinal plane at X^*=0.5.

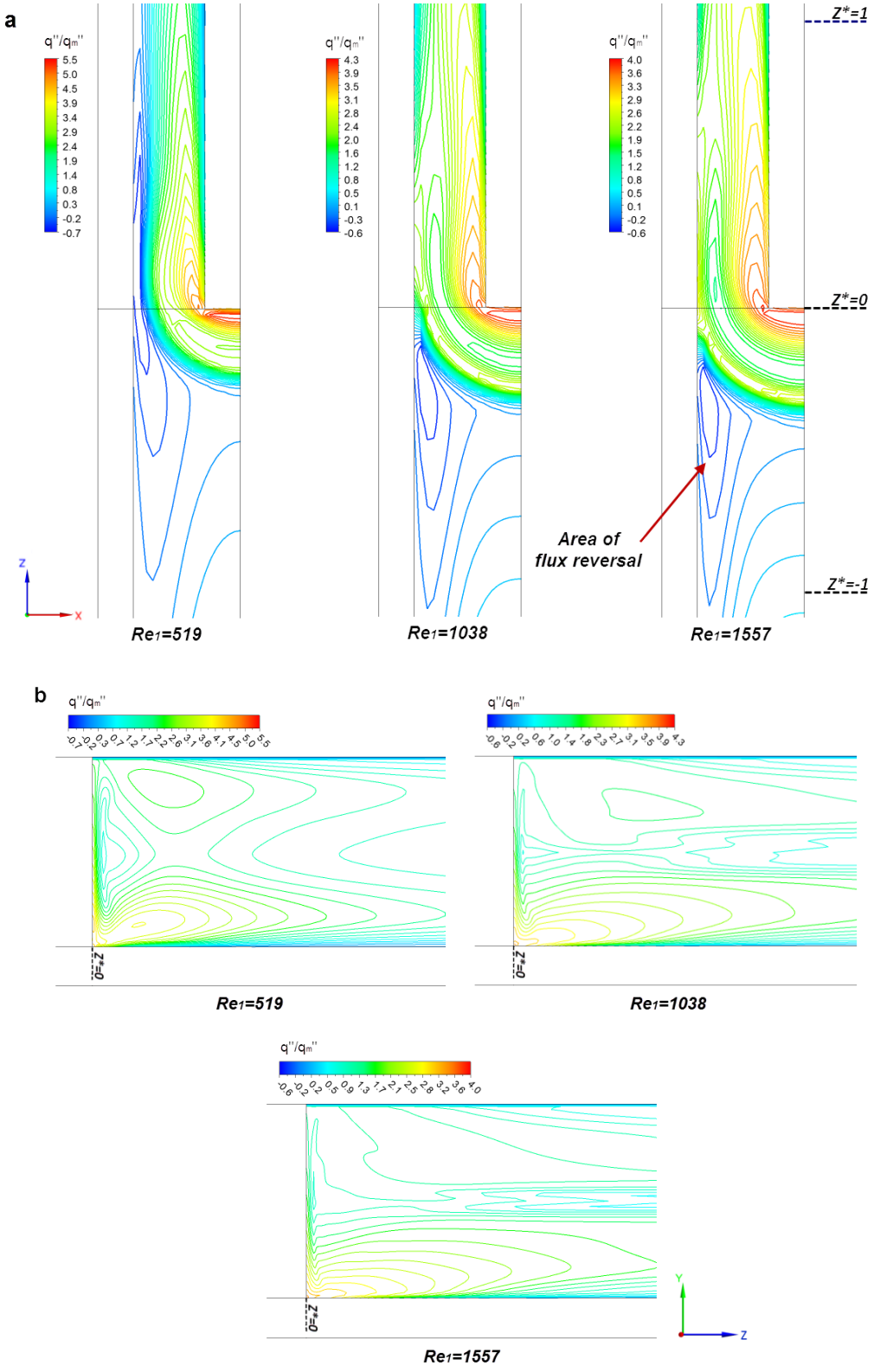

Fig. 14. Wall heat flux contours at the contraction region: (a) Channel bottom wall, (b) fin sidewall.

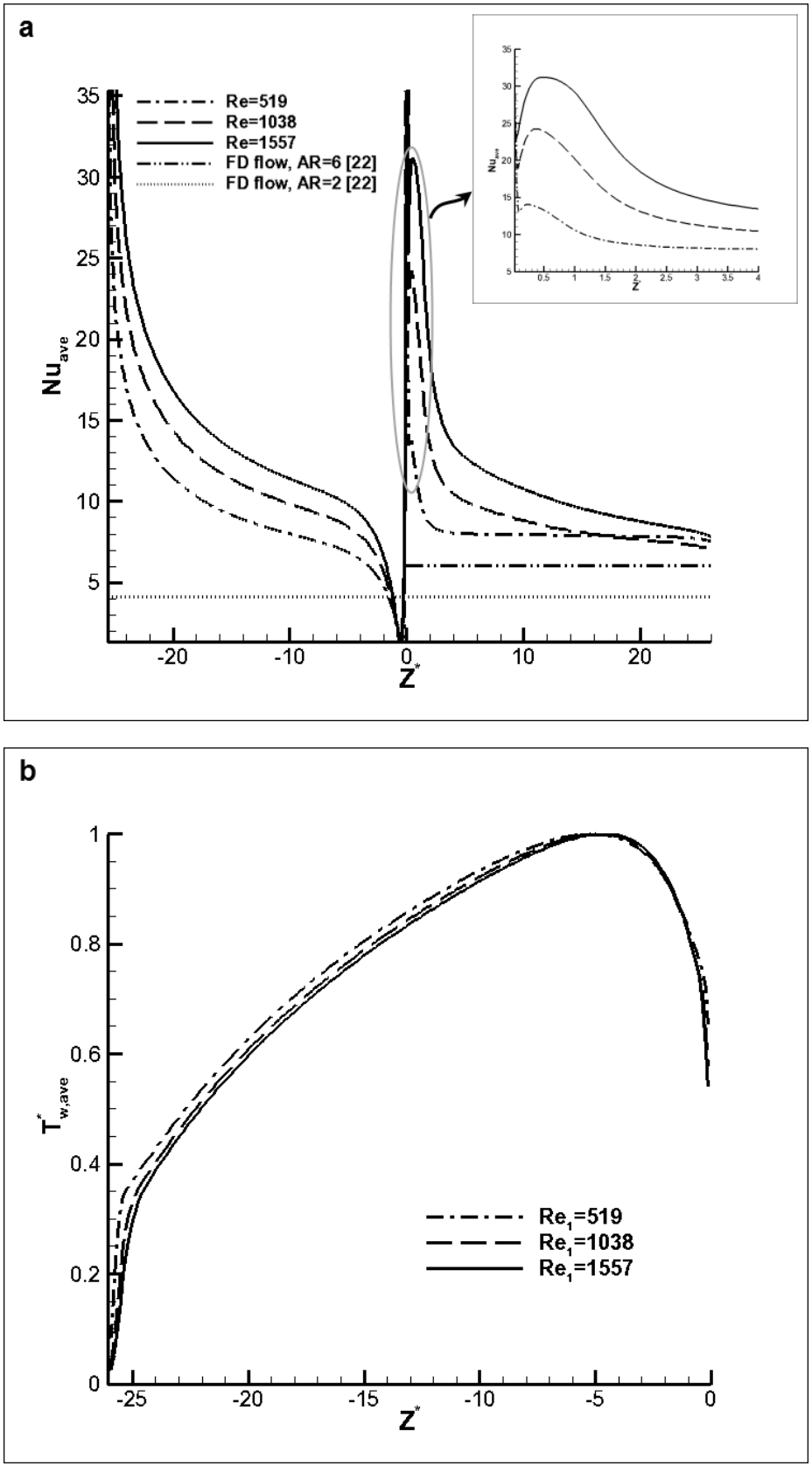

Fig. 15. (a) Circumferentially averaged local Nusselt number distribution against the fully-developed, parallel-flow result, (b) Wall average temperature at heat-sink first section ($Z^*<0$).